Universität Konstanz
FB Informatik und Informationswissenschaft
Master-Studiengang Information Engineering

Masterarbeit

Design and Implementation of a Multispectral Imaging System

zur Erlangung des akademischen Grades eines Master of Science (M.Sc.)

Studienfach:	Information Engineering
Schwerpunkt:	Visual Computing
Themengebiet:	Multispectral Imaging

von

Philipp Ziemer

(01/593684)

Erstgutachter:	Prof. Dr. Dietmar Saupe
Zweitgutachter:	Prof. Dr. Mathias Franz
Betreuer:	Roman Byshko
Einreichung:	März 2013

Acknowledgments

This work was conducted during my study in the field of Information Engineering at the University of Konstanz. During my last years I was especially involved in the workgroup Multimedia Signal Processing of Prof. Dr. Dietmar Saupe. This gave me the opportunity to get further insight into academic research regarding computer science in general and the field of multispectral imaging in detail, which I am very thankful for.

The work conducted would not have been possible without Prof. Dr. Mathias Franz and his workgroup, the institute for optical systems, at the HTWG Konstanz. His workgroup provided all devices used in this thesis. Furthermore, his expertise in digital imaging gave me the guideline to achieve the goal of building a multispectral imaging system.

Many thanks go to my supervisor Roman Byshko, with whom I conducted most of the work. He introduced me to the topic, always provided patient help, and was very dedicated to achieve good results, even if it took many hours of laboratory work.

I want to thank my parents for giving me the opportunity to study. Furthermore all my friends, who I could bore with details of my work. My special thanks go to Anja Leiderer. She always supported me, balancing my moods, and motivated me to continue.

Abstract

Tricolor imaging systems are widely deployed as they produce satisfying results for everyday use. However, for the use in industry, computer graphics, and design, it is important to achieve an even higher level of precision. This can be reached via multispectral images. Instead of three color values, each pixel of such an image contains a whole spectral power distribution.

The aim of this work is to motivate, describe, and build a multispectral imaging system using devices such as a high sensitive camera and a tunable filter. Similar systems have already been reviewed in the literature. The difficulties are to adapt such a system, since the complexity of the different devices and models is high. Furthermore they have to be selected accordingly to the purpose of the system, which is in this case recording spectral images of natural scenes.

Different devices were integrated in a common framework. Especially interesting in this context was the camera API and the process of examining and accessing the recording sequence and exposure settings which will be documented in this thesis. Its functionality had to be synchronized with the filter, in order to automatically record exposure sequences over different wavelengths.

Based on the implementation, the system was calibrated through the use of a monochromator and an integrated sphere. In a series of experiments the light of the monochromator was recorded using a calibrated spectroradiometer and the multispectral imaging system. Through the recorded data the multispectral imaging system could be corrected for noise and hence its characterization—the spectral sensitivity, position of the measurements points on the wavelength axis, and normalization matrix—was achieved. The models were validated in a final experiment.

The result was the attainment of a fully integrated multispectral imaging system. For this system the noise model and the spectral sensitivity are known factors. The finding about this synergy could be used for further research projects.

Table of Contents

List of Figures

List of Tables

Chapter 1

Introduction

It is a well established concept to divide color into a three dimensional space. As long ago as 1853, Hermann Günther Graßmann, a German mathematician and linguist, introduced the idea of describing color with three variables in the book *Theory of Compound Colors*. Thanks to a great number of biological studies about the human perception of color, it is nowadays known that our eyes in fact only rely on three registration constituents. The emergence of computers put this concept to use in an even more significant way. Digital color imaging typically encodes colors in three variables: red, green, and blue.

However, alongside technological progress, several applications emerged that were in the need of identifying spectral power distributions or spectral reflectances which are independent from the environmental influences they are observed under. Due to metamerism, a phenomenom explained in detail during this thesis, this required a description of natural colors with more than three variables. The research field of multispectral imaging was born.

Multispectral cameras offer a lot of advantages over regular three-channel devices. Through them, the whole spectral information of a recorded scene becomes available. This spectral data can then be used to reveal forest canopy features, oil spills or to identify surfaces in general. Furthermore, having obtained the spectral reflectance information of a scene, one can compute the tristimulus values under any given illuminant and for arbitrary observers with a very high color accuracy. Typical use cases for multispectral imaging today are astronomy, medical imaging, remote sensing, digital archiving of paintings or other museum objects, textile industry, printing industry, and many others.

Designing and implementing a multispectral imaging system is of high challenge. Different issues accumulate. First, the adequate devices used for the system itself or for calibration and validation have to be determined. Regular cameras neither provide

enough accuracy nor robustness to image noise. Therefore sophisticated CCD cameras have to be used in order to provide precise measurements. Furthermore, color filters with specific transmittance properties are integrated in the system to record more than three channels. This enables the spectral reconstruction. From the software side, the devices have to be integrated in a common framework.

Beside integrating the system, there are different sophisticated models on which multispectral imaging is based. They estimate the spectral reflectance of surfaces, realizing different concepts and paradigms. The purpose of the multispectral imaging system specifies the kind of the model that should be used.

After having assembled the proper hardware, implemented the APIs into a common framework, and chosen a model the devices have to be evaluated. This evaluation includes the handling of noise of the whole multispectral imaging system, e.g. vignetting or dark current. Afterwards, properties of the system such as its sensitivity to different spectra or the precise position of the channel responses at the wavelength axis have to be examined. This requires substantial experimental effort.

During my master project and thesis I designed and implemented a multispectral imaging system. The work has been accomplished at and with the help of the workgroup *Multimedia Signal Processing* of Prof. Dr. Dietmar Saupe at the University of Konstanz in cooperation with the *Institute for Optical Systems* (IOS) under Prof. Dr. Mathias Franz at the HTWG Konstanz. My adviser for research and experiments was Roman Byshko.

The aim of this work is to motivate, describe, and build a multispectral imaging system using devices such as a high sensitive camera and a tunable filter. Similar systems have already been reviewed in the literature. The difficulties are to adapt such a system, since the complexity of the different devices and models is high. Furthermore they have to be selected accordingly to the purpose of the system, which is is recording spectral images of natural scenes. From this a database of natural spectra can be established, which is of scientific interest for further research.

1.1 Structure of this Thesis

The thesis is structured in two parts. In the first part the theoretical concepts behind multispectral imaging are introduced. It revisits tricolor imaging in order to provide the

knowledge required to understand further concepts and motivate multispectral imaging. After that, the various different mathematical models used in multispectral imaging are examined. They provide an accurate model for the camera and for the estimation of spectral reflectances. Further several devices are addressed which are used to built multispectral imaging systems. Finally I review the important topic of noise and provide methods to compensate for it.

In the second part of this thesis I describe my original work. The different devices and the framework in which the devices are integrated are introduced and their properties discussed. After the initial implementation of the system, the experimental part is given. I present conducted experiments, their results as well as problems arising during the calibration process.

1.2 Related Work

Multispectral color imaging systems are developing rapidly, because of their strong potential in many domains of application. Therefore, many researchers and research groups engage this topic. Some of the work which I found particularly helpful, and will therefore cite throughout this thesis, is listed below. Of course this list is non-exhaustive.

- *Signal and Image Processing Department* at the *Ecole Nationale Supérieure des Télécommunications* (ENST) in Paris, France: Especially Jon Y. Hardeberg published several research papers in the late 1990s. They lead up to his PhD thesis in 1999. He was one of the first scientists using a tunable filter instead of the established filter wheels. This work includes a complete overview of multispectral imaging systems and is often quoted [1, 2, 3, 4, 5].

- *CRISATEL European Union project*: The CRISATEL multispectral acquisition system is dedicated to the digital archiving of fine art paintings. There are many researchers contributing to this project. I especially found the articles and thesis of Alejandro Ribés Cortés very interesting. They compared many of the different mathematical models used in multispectral imaging [6, 7].

- *Institute of Imaging and Computer Vision* at the *RWTH Aachen University* in Aachen, Germany: Under Prof. Dr. Til Aach the group built a multispectral imaging system with previously evaluated filters on a filter wheel. They published

a number of articles on the topic of multispectral high dynamic range imaging since 2008 [8, 9, 10, 11, 12, 13, 14].

Chapter 2

The Visible Spectrum and Tricolor Imaging

Contents

Understanding how humans perceive color is the basis of tricolor imaging. Therefore it is crucial to revisit the descent of perceptible colors. This chapter presents the basic principles about the visible color spectrum which will lead up to the essentials of colorimetric analyses in tricolor imaging. The flaws of these state of the art techniques will be discussed and hence the method of multispectral imaging motivated.

2.1 The Visible Spectrum

Light and color always have been a source of interest for natural scientists. Already Aristotle examined color in a philosophical way and concluded that all of them are a mixture of black and white. However, Sir Isaac Newton's famous prism experiment, explained in the next paragraph, proofed him wrong. This was the birth of modern color science.

In his experiment he showed that white light could be separated into a range of colors through the use of a prism [4]. Due to the *apparition* of different colors, he called this phenomenon spectrum, Latin for apparition. In a later experiment he also proofed that the spectral colors could be recombined to re-create the white light and that an isolated single spectral color is not enough to do so. Figure 2.1 displays the experimental setup. Daylight shines through a hole in wall #1 into prism #1. There it spreads out into the spectral colors. The red spectral color continues through a hole in wall #2 and falls into prism #2. It stays red on wall #3. Soon after the initial publication the term spectrum referred to a plot of light intensity or a power function of wavelengths.

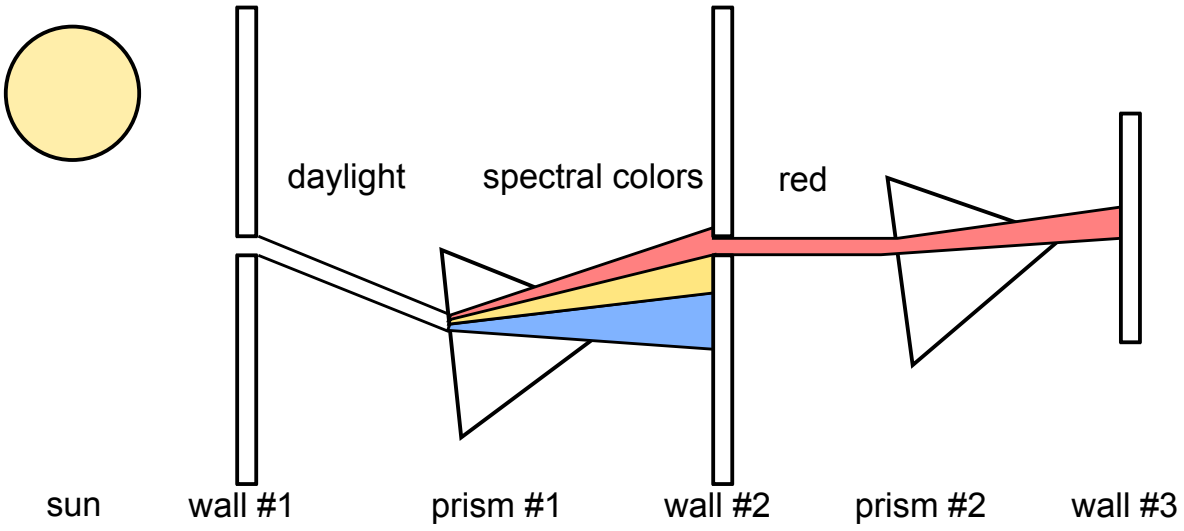

Figure 2.1: Newton's prism experiment.

Spectra typically visible to the human eye lie in a wavelength range from 380 nm to 780 nm. Although other wavelengths can be observed by sophisticated devices as well, this is the range interesting for colorimetric and multispectral imaging. How is the color of a surface generated in detail? Light, or better electromagnetic radiation, plays an important role in this matter.

To evaluate the spectral properties of a surface, it is important to know the *spectral power distribution* (SPD) of the illuminant it is observed under. The SPD of an illuminant is defined as *"the power of a light ray per unit wavelength per unit area perpendicular to the propagating direction"* [15]. By convention, the SPD is normalized to its power at 560 nm. This so-called *spectral radiance* of the illuminant at wavelength λ is given by the function $l(\lambda)$.

By themselves, surfaces of materials have a wide variety of spectral characteristics. These are spectral reflectance, transmission, absorption and scattering [15, p. 14–18]. For simplicity I discuss only the spectral reflectance, the most significant one. It is defined as the ratio of reflected to incident light described by the function $r(\lambda)$. Together with the spectral radiance of the illuminant the spectral radiance f of a surface point is given by

$$f(\lambda) = r(\lambda)l(\lambda). \tag{2.1}$$

This is just a simple equation to describe the spectral properties of a surface. Other attributes, like gloss or roughness, are not adequately modelled here. However, this is enough for our purpose. Figure 2.2 visualizes this simple model for the interaction between illuminant, surface and the final impression.

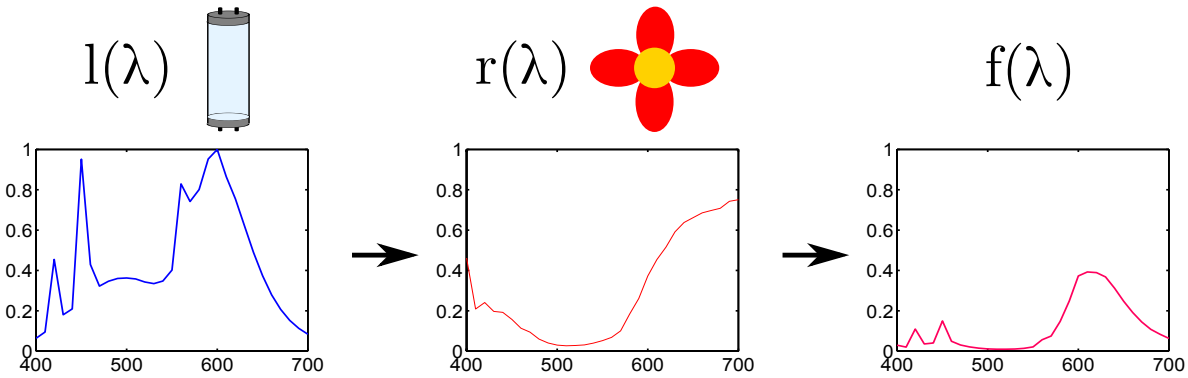

Figure 2.2: Simple model for the reflectance of a surface point with the wavelength on the x-axis and the relative spectral power on the y-axis [4].

2.2 Tricolor Imaging

Before discussing the approach of multispectral imaging, this paragraph focuses on regular tricolor imaging in order to illustrate the boundaries of this technique in comparison to multispectral methods. Tricolor imaging is based on the theoretical framework of colorimetry, the quantification of colors [4]. Colorimetry uses the same principles as the human vision system. For example, an RGB device has three sensors which are sensitive to different aspects of the light, namely red, green, and blue. This can be interpreted as an analogy to the cone cells in the human eye, the S-type for short wavelengths (e.g. blue), the M-type for medium wavelengths (e.g. green) and the L-type for long wavelengths (e.g. red). The cone cells are mainly responsible for the color perception in the human eye during daylight [16].

As a response of a tricolor system, a tristimulus value is obtained which gives an encoding of the perceived color. The spectral sensitivity for the three cones denoted by i is given by $s_i(\lambda)$. The response is constituted through three component vector $\mathbf{c} = [c_1, c_2, c_3]^T$. The following equation builds the basis of colorimetry [17, 4]:

$$c_i = \int_{\lambda_{min}}^{\lambda_{max}} l(\lambda) r(\lambda) s_i(\lambda) d\lambda, \text{ for } i = 1, 2, 3. \tag{2.2}$$

This equation can be rewritten in matrix form

$$\mathbf{c} = \mathbf{S}^T \mathbf{L} \mathbf{r}, \tag{2.3}$$

where $S = [s_1, s_2, s_3]$ is the matrix of the eye sensor sensitivities $s_i = [s_i(\lambda_1)\ s_i(\lambda_2)\ \ldots\ s_i(\lambda_n)]$, with $\lambda_1 = \lambda_{min}$, respectively $\lambda_n = \lambda_{max}$, and the sampling interval $d\lambda = \lambda_j - \lambda_{j-1} = \frac{1}{n-1}(\lambda_{max} - \lambda_{min})$, for $j = 2, \ldots, n$. Further $\mathbf{L}$ is the diagonal illuminant matrix with the samples of $l(\lambda)$ along the diagonal, and $\mathbf{r}$ is a vector of the sampled spectral reflectance of the object. The matrix notation has the advantage to allow the usage of matrix algebra to solve problems related to color.

After translating the sensor response into a three component vector, the tristimulus value, it can be used for further processing. In order to analyze why such a tricolor value is not sufficient, the next part examines color spaces and color difference formulas. These give a first insight into the problems.

2.3 Color Spaces

Associating a tristimulus value with a color is achieved through the usage of color spaces. There are several different color spaces designed by different organizations and companies. Some are presented here by the author's selection.

2.3.1 CIE 1931 XYZ Color Space

One of the very first mathematically defined color spaces is the *CIE 1931 XYZ color space* (CIE XYZ), created by the *International Commission on Illumination* (CIE) in 1931 [15, 17, 18]. It is based on the *CIE RGB color space* (CIE RGB) which is premised on experimental results accomplished by W. David Wright and John Guild in the late 1920s. The model was developed by transforming CIE RGB into a space, which would fulfill several desirable properties, some of which are non-negative values and equality of the color matching functions to others.

The three color matching functions are the numerical descriptions of the chromatic response of the observer. Since the final tristimulus values depend on the observer's field of view, the CIE defined the standard (colorimetric) observer. The tristimulus value $[X, Y, Z]^T$ can be calculated through:

$$\begin{aligned} X &= k \int_{\lambda_{min}}^{\lambda_{max}} f(\lambda)\bar{x}(\lambda)d\lambda \cong k \sum f(\lambda)\bar{x}(\lambda)\Delta\lambda = k \sum l(\lambda)r(\lambda)\bar{x}(\lambda)\Delta\lambda, \\ Y &= k \int_{\lambda_{min}}^{\lambda_{max}} f(\lambda)\bar{y}(\lambda)d\lambda \cong k \sum f(\lambda)\bar{y}(\lambda)\Delta\lambda = k \sum l(\lambda)r(\lambda)\bar{y}(\lambda)\Delta\lambda, \\ Z &= k \int_{\lambda_{min}}^{\lambda_{max}} f(\lambda)\bar{z}(\lambda)d\lambda \cong k \sum f(\lambda)\bar{z}(\lambda)\Delta\lambda = k \sum l(\lambda)r(\lambda)\bar{z}(\lambda)\Delta\lambda, \\ k &= \frac{100}{\int_{\lambda_{min}}^{\lambda_{max}} l(\lambda)\bar{y}(\lambda)d\lambda} \cong \frac{100}{\sum \bar{y}(\lambda)l(\lambda)\Delta\lambda}. \end{aligned} \tag{2.4}$$

The radiance reflectance $f(\lambda)$ from a surface point is known from equation 2.1 together with the spectral radiance of the illuminant $l(\lambda)$ and the object's spectral reflectance $r(\lambda)$. k is a scaling constant and λ_{min} respectively λ_{max} the recording interval. The Y color matching function is called luminance and is exactly equal to the *photopic luminous efficiency function* for the *CIE standard photopic observer*. It gives the perceived brightness of the radiant spectrum. Figure 2.3 displays the three color matching

functions.

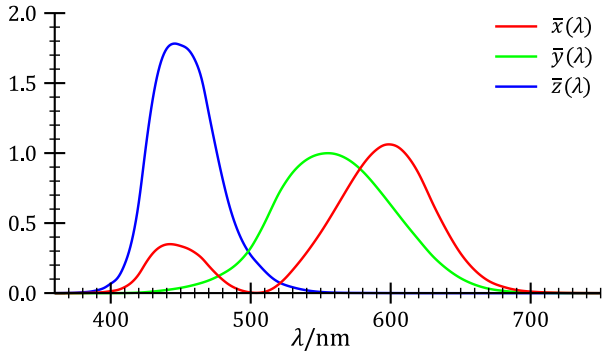

Figure 2.3: The CIE XYZ color matching functions under the standard observer [19].

The CIE XYZ is the basis for all other color spaces which are used in practice and is defined by the CIE. For example the *standard-RGB* (sRGB) created by *Microsoft* and *Hewlett-Packard* in 1996 for the use with monitors, printers, and the Internet is a linear combination of the CIE XYZ [20, 21]:

$$\begin{bmatrix} R_{sRGB} \\ G_{sRGB} \\ B_{sRGB} \end{bmatrix} = \begin{bmatrix} 3.2410 & -1.5374 & -0.4986 \\ -0.9692 & 1.8760 & 0.0416 \\ 0.0556 & -0.2040 & 1.0570 \end{bmatrix} \begin{bmatrix} X \\ Y \\ Z \end{bmatrix} \tag{2.5}$$

These numerical values match those in the official sRGB specification and differ slightly from those in the original publication. The corresponding original XYZ values are such that white is D65 with unit luminance under the CIE 1931 standard observer. For different viewing conditions the matrix has to be adapted.

2.3.2 CIELAB

Even though the XYZ color space proofed to be very useful for the quantification of color stimuli it has a major flaw. Quan summarized this in the following statement: *"[...] the length of segments, which represent equal perceived difference in the blue region differ from those in the green region by a factor of five. In a uniform color space they ought to have the same length"* [15, p. 21–22]. This means that working with this concept produces equal distances in various parts of the color space representing different perceptual color differences.

The CIELAB is a uniform color space derived from the CIE XYZ color space through

cube root transformation [21]. It is designed to overcome the cited problems. Much research effort has been put into the transformation. Although there are other uniform color spaces like CIELUV, CIELAB is mostly used today. The three CIELAB values used for describing a point in the color space are L^*, a^*, and b^*. In the plane negative a^* represents green, positive a^* red, negative b^* blue and positive b^* yellow. The larger the absolute value in negative or positive direction the more saturated is a color. The L^* value gives the brightness on a scale from 0 (dark) to 100 (bright). The larger the value the brighter the color. Figure 2.4 provides a good overview how CIELAB values are distributed.

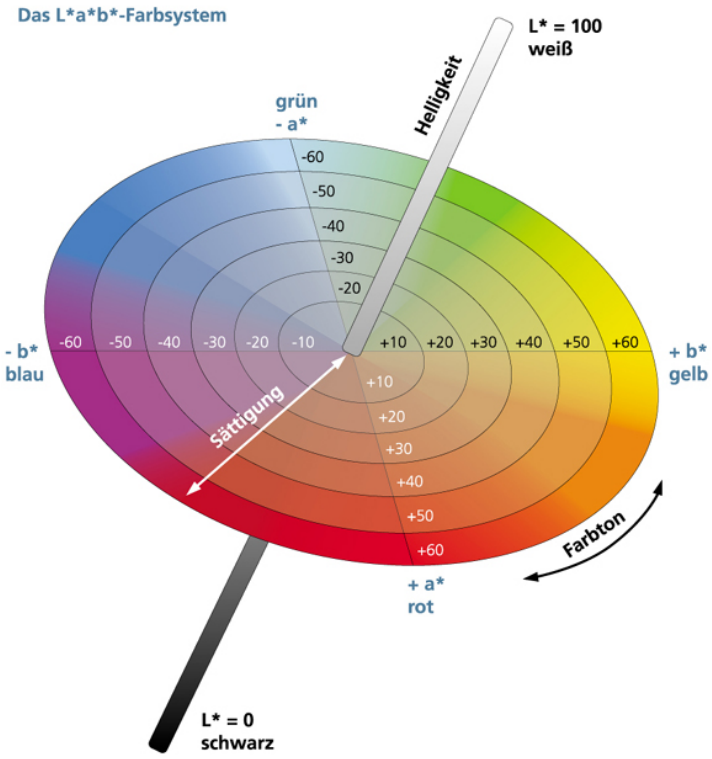

Figure 2.4: The CIELAB color scale [22].

The coordinate values are transformations of the the tristimulus values X, Y and Z:

$$\begin{aligned} L^* &= 116 f(Y/Y_w) - 16, \\ a^* &= 500[f(X/X_w) - f(Y/Y_n)], \\ b^* &= 200[f(Y/Y_w) - f(Z/Z_n)], \end{aligned} \tag{2.6}$$

where X_w, Y_w and Z_w are the tristimulus values for the reference white. Function f is

defined as:

$$\begin{aligned} f(x) &= 7.787x + \frac{16}{116} \quad \text{for} \quad x \leq 0.008856, \\ f(x) &= x^{\frac{1}{3}} \qquad\qquad\quad \text{for} \quad x > 0.008856. \end{aligned} \tag{2.7}$$

The CIELAB color space is relatively simple and straightforward. Even though it was designed to overcome all problems it is not perfectly uniform but just a good approximation. Furthermore the different environmental factors affecting color perception, for example illuminant, are not included in the transformation. Still it is the most used color space by researchers and sophisticated software. The next section describes different metrics using the CIELAB color space.

2.3.3 Color Difference Formulas

There are several different color difference formulas specified by the CIE for CIELAB [23, 24]. The most generic one is the *CIE76*. For two color values $C_1 = (L_1^*, a_1^*, b_1^*)$ and $C_2 = (L_2^*, a_2^*, b_2^*)$ two colors differ by:

$$\Delta E_{ab}^* = \sqrt{(L_2^* - L_1^*)^2 + (a_2^* - a_1^*)^2 + (b_2^* - b_1^*)^2}. \tag{2.8}$$

This is the Euclidean distance in the CIELAB color space. A value of $E_{ab}^* \approx 2.3$ corresponds to a *just noticeable difference* (JND). A JND is defined as the smallest noticeable difference between two sensor stimuli.

To address the non-uniformities in the CIELAB color space due to the previously mentioned reasons, *CIE94* was specified by the CIE, which brought several adaptions. It is defined for the $L^*C^*h^*$ color space. This color space is directly derived from CIELAB describing lightness, chroma and hue. Nevertheless CIE94 did still not sufficiently resolve the issue. Therefore *CIEDE2000* was specified, introducing five corrections: A hue rotation term dealing with the problematic blue regions, compensation for neutral colors and compensation for lightness, chroma and hue.[1].

[1]The interested reader can find the corrected formula it the article *"The CIEDE2000 Color-Difference Formula"* by Gaurav Sharma, Wencheng Wu and Edul N. Dalal [25].

2.4 Limits of Tricolor Imaging

Tricolor imaging is present in every day life on posters, computer-, television- and mobile-displays. For general purposes it is sufficient and well adapted. However, using more proficient applications, problems arise. This has several reasons. First I focus on metamerism, as it is the main cause of inaccuracies in the image reproduction workflow.

2.4.1 Metamerism

A good definition for metamerism is given by Foster et al: *"Metamerism is the phenomenon of lights appearing the same to the eye, or, more generally, the sensor system, but having different spectral radiant power distributions over the visible spectrum"* [26, page 2359]. But why do metamers arise? They are caused by the difference between the color spectra and the color perception of general sensor systems, in our case the human eye or a camera.

Since reflectance spectra are continuous functions and the sensor response (given in equation 2.2) only has three values, it is clear that there exist different spectra mapped to the same response. Therefore they appear the same to the human eye. Regarding one object, the spectral radiance of the surface does not change. Hence, metamerism depends only on the illuminant. In colorimetry terms this means that different illuminants produce equal tristimulus values. Figure 2.5 gives an example of metamerism. Daylight reflected from a violet flower has a different spectral power distribution than an image of the flower displayed at a computer monitor, which is adjusted to match the color of the flower.

Metamerism is of high importance to modern image displays. Without it, there would be no filming, photography or printing as known by nowadays society. These technologies rely on matching the spectral distributions of the original scene to the spectral distribution of the reproduced image, so they appear the same to the human eye. With the current technology it would be impossible to emit the exact same spectrum. But metamerism can also be a disadvantage for the industry or researchers, namely if different surfaces, appearing the same under one illuminant, become distinguishable under another. Visual identity is then no longer a guide to surface identity.

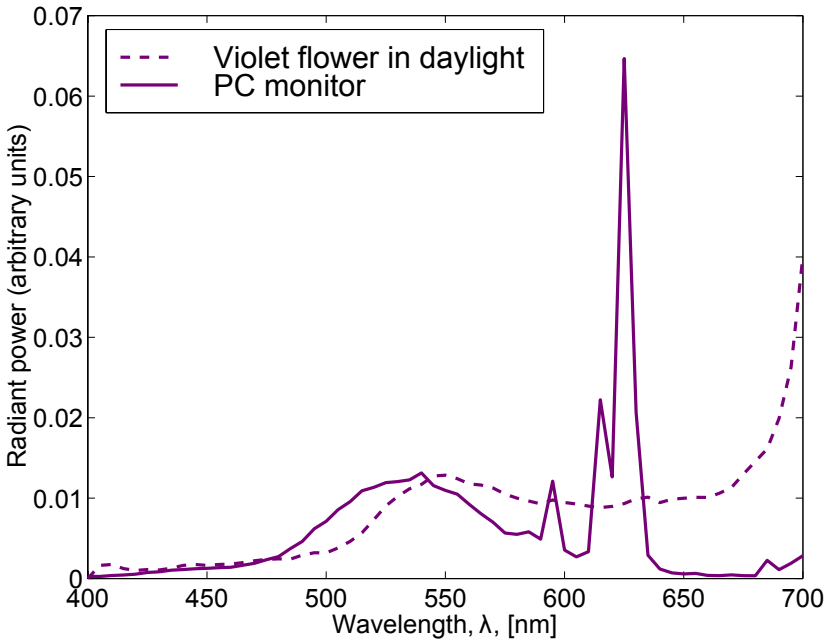

Figure 2.5: Example of metamers [3].

2.4.2 Metameric Image Reproduction Workflow

Viewing the image reproduction workflow for metameric devices provides the answer why tricolor imaging is not precise. All problems arise to the previously discussed standards. The overall color reproduction error is not due to one step, but to the overall reproduction process. Figure 2.6 shows different steps during the reproduction. A detailed explanation, as given by [27], will follow summing up this chapter.

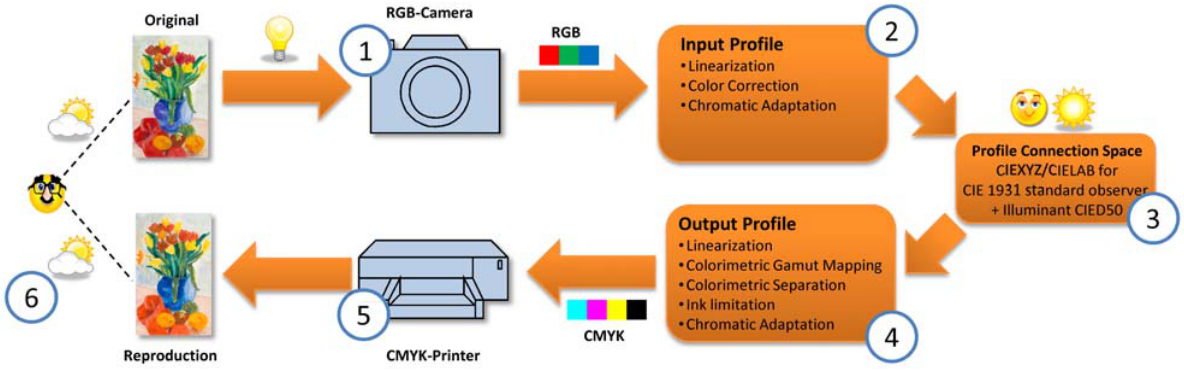

Figure 2.6: Metameric image reproduction workflow [27].

1. **Camera/Scanner System:** Recording a continuous spectral radiance with a regular tricolor device results in only three values. All further information of the

shape of the curve is lost. Different reflectances can result in the same sensor response and metamerism occurs. Since most devices are not linear dependant on human color matching functions, but their own, a human observer would be able to distinguish the colors under the same viewing conditions. It becomes impossible to reproduce these colors accurately.

2. **Input Profile:** The sensor response of the recording device is transformed into the *profile connection space* (PCF). This is usually the CIE XYZ or CIELAB color space under illuminant CIE D50 and CIE 1931 standard observer. The transformation process is in general ambiguous, since the acquisition illuminant is usually different from CIE D50. This leads to additional information loss.

3. **Profile Connection Space:** As mentioned, the color spaces are designed for the CIE 1931 standard observer under illuminant CIE D50. A real illuminant and observer normally will not agree with this standard. The difference in illumination leads to illumination metamerism which causes further problems. Colors not distinguishable by the camera could be under CIE 1931 standard observer for CIE D50 and vice versa.

4. **Output Profile:** The output profile of the printer describes the transformation between the PCS and the control values of the printing device, e.g. CMY or CMYK. If again the illuminant of the acquisition is still different to CIE D50, similar problems related to illuminant metamerism occur.

5. **Printing System:** The set of possible colors which can be printed by the system are small compared to all colors in nature. A perfect reproduction is impossible for most printers, although sophisticated algorithms can reduce the error. Further the small spectral variability of the used inks, mostly CMY or CMYK, does not allow reproductions that match under multiple illuminants.

6. **Viewing Condition:** Since real observers differ from CIE 1931 standard observer and the real illuminants typically have different spectral radiances than CIE D50, a metameric mismatch is possible under real viewing conditions.

2.5 Conclusion

Figure 2.7 points out what is the real problem with tricolor imaging—is the cross green or blue? The impression is always a matter of context. This context could be the conditions an image is taken or viewed under. Further there are many problems and flaws in storing and reproduction. Sampling a curve to just three values and using predefined color spaces leads to different results in original scenes and reproduced images. Still tricolor imaging is sufficient for many applications. However, if the real surface identity is relevant, the only solution is multispectral imaging systems using more than just three channels and a spectral representation for surfaces.

Figure 2.7: Two crosses printed with the same color [4].

Chapter 3

Theoretical Principles of Multispectral Imaging Systems

Contents

The previous chapter showed that for a conventional three channel system it is impossible to reproduce color in an accurate way. A *multispectral Imaging System*, however, is able to achieve a higher accuracy through producing a sampled spectral curve of a recorded spectral radiance. Although such kind of system per se is not independent from viewing conditions, i.e. in respect to the illuminant, it is a great improvement and superior to other systems. Furthermore, if information about the illuminant is available, real independence can be achieved. In such case the system allows to distinguish whether a picture of a red object is taken under white light or a picture of a white object is taken under red light - a differentiation that is impossible under customary conditions. Chapter three discusses the theoretical principles behind these multispectral imaging systems.

3.1 System Model and Spectral Reflectance Estimation

A Multispectral imaging system is very similar to a regular camera. The crucial difference is the possession of more than three channels, which generates a spectral representation over a tristimulus value. Research groups commonly build multispectral imaging systems by the usage of non-masked couple charged device (CCD) cameras and several optical filters for the different channels [1, 6, 28]. The filter allows solely one bandwidth to pass and the camera acquires a greyscale image of the stimulus. Several of these images together assemble to a multispectral image. Figure 3.1 provides a graphical representation of a multispectral imaging system.

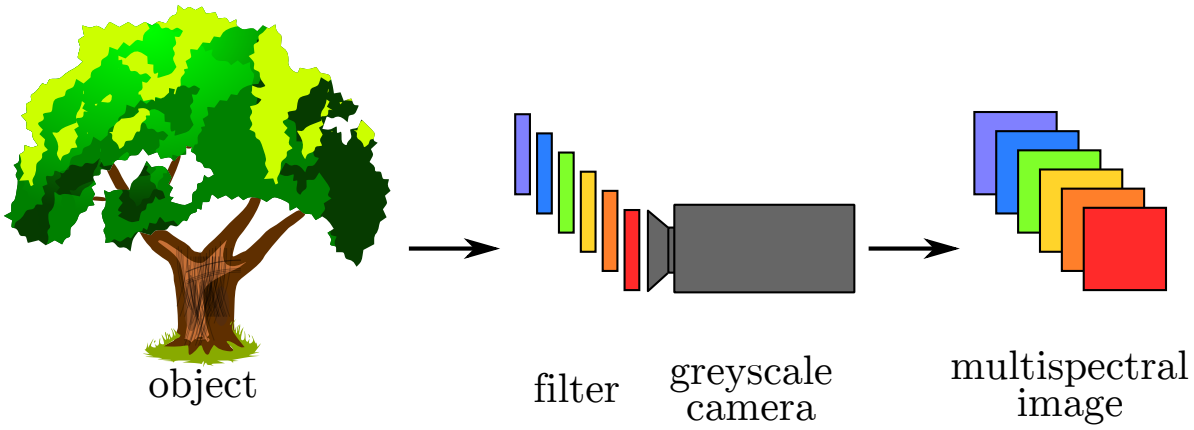

Figure 3.1: Graphical representation of a multispectral imaging system.

The equation for the camera response for such a system is similar to equation 2.2 given in section 2.2. The different components involved are shown in Figure 3.2. There again the spectral radiance of the illuminant is $l(\lambda)$ and the spectral reflectance of the object is $r(\lambda)$. Additionally, one finds the spectral transmittance of the camera lens $o(\lambda)$, the spectral transmittance of the i-th optical filter $\phi_i(\lambda)$, and the spectral sensitivity of the CCD array $\alpha(\lambda)$.

This leads to the following equation for the sensor response a_i for one image pixel at the i-th channel:

$$a_i = \int_{\lambda_{min}}^{\lambda_{max}} l(\lambda)r(\lambda)\phi_i(\lambda)o(\lambda)\alpha(\lambda)d\lambda, \tag{3.1}$$

where $i = 1, \ldots, m$. For every channel, there is a sensor response a_i to describe the spectral properties of an object. In order to be able to calculate the spectral reflectance

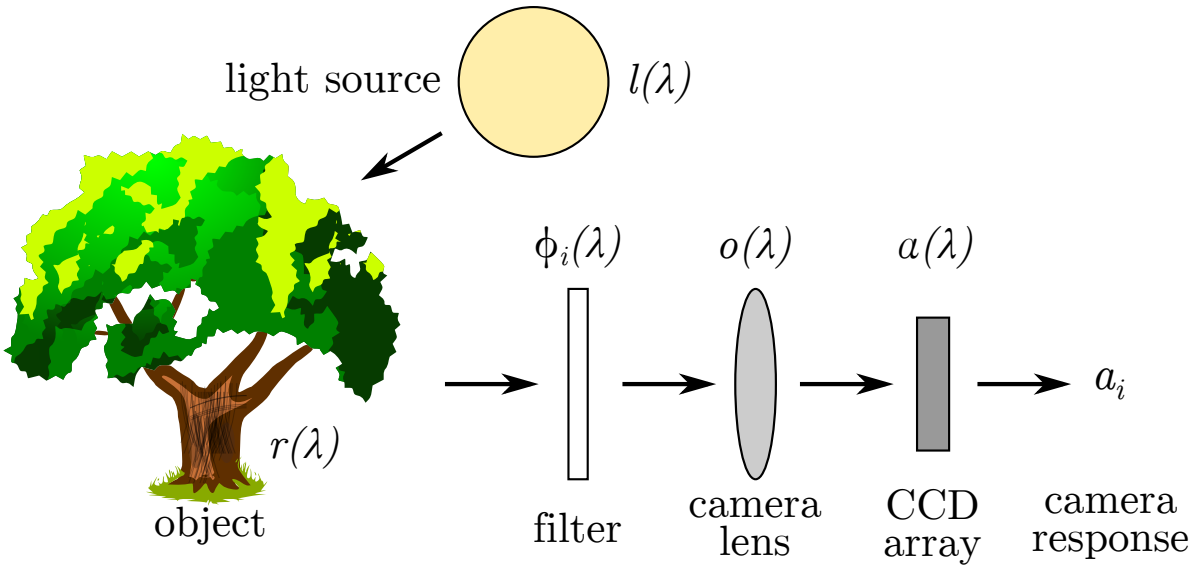

Figure 3.2: Schematic view of a multispectral imaging system.

function $r(\lambda)$, the dependency on other factors has to be removed. The spectral reflectance function supplies a continuous function of a surface point. This is the object's contribution to the perception of the color and the part which is crucial for many applications. It depends exclusively on the physical properties of the object. It does never change as long as the object stays the same. Regular cameras do not estimate $r(\lambda)$, but instead the final color appearance a_i. This is one of the reasons for a metameric image reproduction workflow.

In order to estimate the spectral reflectance of the object, equation 3.1 can be adapted:

$$a_i = \int_{\lambda_{min}}^{\lambda_{max}} r(\lambda) s_i(\lambda) d\lambda, \tag{3.2}$$

where $i = 1, \ldots, m$ and the spectral sensitivity for the i-th channel is given as $s_i(\lambda) = l(\lambda)\phi_i(\lambda)o(\lambda)\alpha(\lambda)$.

By uniformly sampling the spectra at n equal wavelength intervals, this equation can be rewritten in matrix notation using the scalar product:

$$a_i = \mathbf{s}_i^T \mathbf{r}, \tag{3.3}$$

where $\mathbf{r} = [r(\lambda_1) \ldots r(\lambda_n)]^T$ contains the sampled spectral reflectance function and $\mathbf{s}_i = [s_i(\lambda_1) \ldots s_i(\lambda_n)]$ the sampled spectral sensitivity of the i-th channel. The vector $\mathbf{a}$,

representing the sensor response of all m filters, is given as:

$$\mathbf{a} = \mathbf{\Theta r}, \tag{3.4}$$

where $\mathbf{\Theta} = [s_i(\lambda_j)]^T$ is the $m \times n$ matrix of spectral sensitivities. The matrix element at the i-th row and the j-th column contains the spectral sensitivity of the i-th channel at the j-th sampled wavelength.

At this point it should be noted that the model is only accurate for one illuminant. The same illuminant has to be used in a later step for calibration and scene acquisition in order to retrieve the correct spectral reflectance. Such a model achieves the highest accuracy under laboratory conditions, as for example when archiving paintings. My own work focuses on retrieving a channel sensitivity matrix which is independent from the illuminant. The necessary methods are discussed in chapter 7 (see section 7.5). The channel sensitivity matrix is altered only by removing $l(\lambda)$, thus the mathematical models for spectral reconstruction stay the same and are valid for my purposes.

3.2 Spectral Reconstruction

The process of computing the actual spectral reflectance of objects from the sensor response is called spectral reconstruction. There are many different approaches about what the actual mathematical model for spectral reconstruction could look like [1, 6, 28, 7].

The problem formulated in the sense of equation 3.4 is the way of retrieving the spectrophotometric information $\mathbf{r}$ from the camera response $\mathbf{a}$. It leads up to reformulating the problem as an inverse of $\mathbf{\Theta}$:

$$\mathbf{r}' = \mathbf{Qa}, \tag{3.5}$$

where $\mathbf{Q}$ is the inverse matrix that minimizes the distance $d(\mathbf{r}, \mathbf{r}')$ for an error metric d. Since $\mathbf{\Theta}$ is in general not a square matrix of full rank, first a short excursion to the algebraic *pseudo inverse* is necessary, which will be used for direct and indirect spectral reconstruction methods.

3.2.1 Pseudo Inverse

For the matrix $\mathbf{\Theta}$ to be square, the number of filters would have to be the number of wavelength sampling intervals over the spectrum recorded. In that case, $\mathbf{\Theta}^{-1}$ could be calculated if $\mathbf{\Theta}$ had full rank. The first condition is not met in general. Hence, the pseudo inverse has to be used to solve the problem for a general linear equation system

$$\mathbf{b} = \mathbf{A}\mathbf{x}, \tag{3.6}$$

where $\mathbf{x}$ and $\mathbf{b}$ are vectors and $\mathbf{A}$ is an arbitrary $m \times n$ matrix. If $\mathbf{A}$ is square and non-singular the solution is simply $\mathbf{A}^{-1}\mathbf{b}$.

For the overdetermined case $m > n$, no solution $\mathbf{x}$ exists for this set of equations [29]. The task is now to find a vector $\mathbf{x}$ that minimizes the norm $\|\mathbf{A}\mathbf{x} - \mathbf{b}\|^2$. The product $\mathbf{A}\mathbf{x}$ varies over the complete columns space of $\mathbf{A}$, so the closest vector to $\mathbf{b}$ with respect to a vector norm has to be found that lies in there. If $\mathbf{x}$ is the solution to this problem, the difference $\mathbf{A}\mathbf{x} - \mathbf{b}$ must be orthogonal to the column space of $\mathbf{A}$ and hence $\mathbf{A}^T(\mathbf{A}\mathbf{x} - \mathbf{b}) = 0$, indicated by the following equation:

$$\mathbf{A}^T\mathbf{b} = (\mathbf{A}^T\mathbf{A})\mathbf{x}. \tag{3.7}$$

This set is called the *normal equations*. Solving the equations leads to the least square solution of $\|\mathbf{A}\mathbf{x} - \mathbf{b}\|^2$ with respect to $\mathbf{x}$:

$$(\mathbf{A}^T\mathbf{A})^{-1}\mathbf{A}^T\mathbf{b} = \mathbf{x}'. \tag{3.8}$$

If $\mathbf{A}^T\mathbf{A}$ is of full rank, the pseudo inverse for overdetermined linear equation system is expressed as:

$$\mathbf{A}^+_{over} = (\mathbf{A}^T\mathbf{A})^{-1}\mathbf{A}^T. \tag{3.9}$$

When the system is underdetermined, thus $m < n$, there are fewer constraints than unknowns. This leads to a set of equations with infinite solutions. It remains to pick the smallest one of these. The vector $\mathbf{x}$ will be minimized to the constraint $\mathbf{b} = \mathbf{A}\mathbf{x}$. This is done by *Lagrange Multipliers* which allows adding the term to the quantity to be minimized:

$$\|\mathbf{x}\|^2 + \lambda^T(\mathbf{b} - \mathbf{A}\mathbf{x}) = 0. \tag{3.10}$$

Derivating with respect to $\mathbf{x}$ gives:

$$2\mathbf{x} - \mathbf{A}^T\lambda = 0. \tag{3.11}$$

To solve for λ, the equation has to multiplied by $\mathbf{A}$ in order to make the term square. Through this one obtains

$$2\mathbf{A}\mathbf{x} - \mathbf{A}\mathbf{A}^T\lambda = 0. \tag{3.12}$$

Together with $\mathbf{b} = \mathbf{A}\mathbf{x}$ one solves for λ:

$$2\mathbf{b} = \mathbf{A}\mathbf{A}^T\lambda \Leftrightarrow \lambda = 2(\mathbf{A}\mathbf{A}^T)^{-1}\mathbf{b}. \tag{3.13}$$

Equation 3.13 can be used in equation 3.11 to solve the initial problem, hence

$$\mathbf{x} = \mathbf{A}^T(\mathbf{A}\mathbf{A}^T)^{-1}\mathbf{b}, \tag{3.14}$$

which leaves for the pseudo inverse in the underdetermined case:

$$\mathbf{A}^+_{under} = \mathbf{A}^T(\mathbf{A}\mathbf{A}^T)^{-1}. \tag{3.15}$$

3.2.2 Direct Methods

Subsequently, the pseudo inverse operator is clarified before put into use. The first set of methods includes the direct spectral reconstruction. In this case the matrix $\mathbf{\Theta}$ is known. It represents a physical characterization of the multispectral imaging system. It requires measurements of the CCD sensitivity, the filter transmittance, and the optics transmittance. Luckily this can be done all together, since the multispectral imaging system is one unity and therefore all components are characterized together in $\mathbf{\Theta}$. If one device is changed the calibration process has to be repeated. After the characterization, the matrix $\mathbf{\Theta}$ can be obtained directly from the measurements.

The value $\mathbf{r}$ is obtained in equation 3.4 with $\mathbf{\Theta}$ being a known $m \times n$ matrix. The i-th row of this matrix represents the sensitivity of the i-th channel, where $i = 1 \ldots m$. The j-th column corresponds to the j-th wavelength interval, where $j = 1 \ldots n$. Since there are less channels than samples ($m < n$), $\mathbf{r} = \mathbf{\Theta}\mathbf{a}$ is an underdetermined linear equation

system, hence an approximation $\mathbf{r}'$ which minimizes the distance as:

$$\begin{aligned} \mathbf{r}' &= \mathbf{\Theta}^{+}_{under}\mathbf{a} \\ &= \mathbf{\Theta}^{T}(\mathbf{\Theta}\mathbf{\Theta}^{T})^{-1}\mathbf{a}. \end{aligned} \tag{3.16}$$

This leaves for the pseudo inverse in the direct case:

$$\mathbf{Q}_{direct} = \mathbf{\Theta}^{T}(\mathbf{\Theta}\mathbf{\Theta}^{T})^{-1} \tag{3.17}$$

This is the basic method for direct spectral reconstruction. However it does not account for noise and does not guarantee the spectra $\mathbf{r}$ and its estimation $\mathbf{r}'$ to be close, but only that their projections into the response space of the multispectral imaging system are. This may lead to very sharp spectral curves that are not natural or even curves that do not actually describe a real spectrum [28]. Due to this divergences more sophisticated methods were developed which will be presented next.

3.2.2.1 Smoothing Inverse

Smoothing inverse is often used in linear regularization and can be adapted for spectral reconstruction as well as to smoothen the spectral curve [6, 28]. For multispectral imaging it was introduced in the context of the similar problem of spectral radiance estimation by Mancill and Pratt [30] and later adapted by König and Präfcke for spectral reconstruction [31].

To achieve the smoothing effect, a linear transformation Δ_2 is applied to the original spectral reflectance $\mathbf{r}$ and its inverse Δ_2^{-1} to the imaging process matrix $\mathbf{\Theta}$. Applied to equation 3.4 this looks as follows:

$$\mathbf{a} = \mathbf{\Theta}\Delta_2^{-1}\Delta_2\mathbf{r}. \tag{3.18}$$

The idea behind is to calculate the $2nd$ derivation of the reflectance, apply the pseudo inverse, and undo the calculation by applying the inverse. This leads to the smallest norm of the derivation, and hence to an estimation with maximal smoothness, while the pseudo inverse only finds an optimal solution in the mathematical sense that is not necessarily a real spectrum.

The matrix Δ_2 can be obtained through the definition of the $2nd$ derivation of a re-

flectance $r(\lambda_j)$ with respect to λ_j [28]:

$$\begin{aligned} r''(\lambda_j) &= r'(\lambda_{j+1}) - r'(\lambda_j) \\ &= r(\lambda_{j+2}) - r(\lambda_{j+1}) - (r(\lambda_{j+1}) - r(\lambda_j)) \\ &= r(\lambda_{j+2}) - 2r(\lambda_{j+1}) + r(\lambda_j). \end{aligned} \tag{3.19}$$

This equation can be written in matrix form as follows:

$$\mathbf{r}'' = \begin{bmatrix} r''(\lambda_1) \\ \vdots \\ r''(\lambda_{j-2}) \end{bmatrix} = \underbrace{\begin{bmatrix} 1 & -2 & 1 & 0 & 0 & 0 & \dots & 0 \\ 0 & 1 & -2 & 1 & 0 & 0 & \dots & 0 \\ 0 & 0 & 1 & -2 & 1 & 0 & \dots & 0 \\ \vdots & & & & & & & \vdots \\ 0 & 0 & \dots & 0 & 1 & -2 & 1 & 0 \\ 0 & 0 & 0 & \dots & 0 & 1 & -2 & 1 \end{bmatrix}}_{=\Delta_2} \begin{bmatrix} r(\lambda_1) \\ \vdots \\ r(\lambda_j) \end{bmatrix}, \tag{3.20}$$

where Δ_2 is a $(n-2) \times n$ matrix. Unfortunately this matrix is just of rank $n-2$ and therefore it cannot be inverted. To achieve this, two linear independent lines are added that have a minor impact on the derivates:

$$\Delta_2' = \Delta_2 + \varepsilon \mathbf{I}, \tag{3.21}$$

where e.g. $\varepsilon = 10^{-6}$.

Equation 3.21 can now be used in equation 3.18 to built the smoothing inverse:

$$\begin{aligned} \boldsymbol{\Theta}\Delta_2'^{-1}\Delta_2'\mathbf{r} &= \mathbf{a} \\ \Delta_2'\mathbf{r} &= (\boldsymbol{\Theta}\Delta_2'^{-1})^T(\boldsymbol{\Theta}\Delta_2'^{-1}(\boldsymbol{\Theta}\Delta_2'^{-1})^T)^{-1}\mathbf{a} \\ \mathbf{r} &= \Delta_2'^{-1}(\boldsymbol{\Theta}\Delta_2'^{-1})^T(\boldsymbol{\Theta}\Delta_2'^{-1}(\boldsymbol{\Theta}\Delta_2'^{-1})^T)^{-1}\mathbf{a} \\ &= \Delta_2'^{-1}\Delta_2'^{-T}\boldsymbol{\Theta}^T(\boldsymbol{\Theta}\Delta_2'^{-1}\Delta_2'^{-T}\boldsymbol{\Theta}^T)^{-1}\mathbf{a} \\ &= (\Delta_2'^T\Delta_2')^{-1}\boldsymbol{\Theta}^T(\boldsymbol{\Theta}(\Delta_2'^T\Delta_2')^{-1}\boldsymbol{\Theta}^T)^{-1}\mathbf{a}. \end{aligned} \tag{3.22}$$

This leads to the following equation for the smoothing inverse:

$$\mathbf{Q}_s = \underbrace{(\Delta_2'^T\Delta_2')^{-1}}_{=\mathbf{N}_s}\boldsymbol{\Theta}^T(\boldsymbol{\Theta}\underbrace{(\Delta_2'^T\Delta_2')^{-1}}_{=\mathbf{N}_s}\boldsymbol{\Theta}^T)^{-1}, \tag{3.23}$$

where N_s is the $n \times n$ norm-matrix. An alternative to smoothing inverse is the *Wiener inverse* used in *Wiener's filter* which will be discussed next. It represents another direct calculation of the matrix $\mathbf{Q}$ through $\mathbf{\Theta}$.

3.2.2.2 Wiener's Filter

The approach used in Wiener's filter is similar to the one previously presented. But instead of applying the smallest norm of the derivates to smoothen the spectral curve, stochastic values are included in the calculations. These stochastic values describe the correlation of neighboring values in the spectrum. Since spectral curves are smooth, these neighboring values have indeed a high correlation. As the smoothing inverse it was introduced by Mancill and Pratt [30] and later adapted by König and Präfcke.

The basic mathematical derivation for the Wiener inverse $\mathbf{Q}_w$ is the same as for the smoothing inverse [28]. The normalization matrix $N_s = (\Delta_2'^T \Delta_2')^{-1}$ is replaced by another norm-matrix N_w. This correlation matrix models the stochastic values through a correlation coefficient which is exponentiated over the n observation points:

$$\mathbf{N}_w^{-1} = \begin{bmatrix} 1 & \rho & \rho^2 & \dots & \rho^{n-1} \\ \rho & 1\rho & \rho & \dots & \rho^{n-2} \\ \rho^2 & \rho & 1 & \dots & \rho^{n-3} \\ \vdots & & & & \vdots \\ \rho^{n-1} & \rho^{n-2} & \rho^{n-3} & \dots & 1 \end{bmatrix}. \tag{3.24}$$

A good value for the estimation of spectral reflectances is $\rho \approx 0.99$. This changes equation 3.23 as follows:

$$\mathbf{Q}_w = \mathbf{N}_w^{-1}\mathbf{\Theta}^T(\mathbf{\Theta}\mathbf{N}_w^{-1}\mathbf{\Theta}^T)^{-1}, \tag{3.25}$$

where $\mathbf{Q}_w$ is the Wiener inverse.

The Wiener inverse can further be optimized for a given spectral dataset $\mathbf{R}$. Instead of using the norm matrix $\mathbf{N}_w^{-1}$ an autocorrelation matrix is used:

$$\mathbf{R}_{rr}^{-1} = \mathbf{R}\mathbf{R}^T, \tag{3.26}$$

where

$$\mathbf{R} = \begin{bmatrix} r_1(\lambda_1) & r_2(\lambda_1) & \dots & r_m(\lambda_1) \\ r_1(\lambda_2) & r_2(\lambda_2) & \dots & r_m(\lambda_2) \\ \vdots & & & \vdots \\ r_1(\lambda_n) & r_2(\lambda_n) & \dots & r_m(\lambda_n) \end{bmatrix} \tag{3.27}$$

is a $n \times m$ matrix containing the m sampled wavelength intervals and the n spectral reflectances $\mathbf{r_j}$.

In practice the Wiener inverse performs quite similar to the smoothing inverse. The main advantage is that modelling of the noise can be included right away through a noise correlation matrix $\mathbf{R}_{nn}$:

$$\mathbf{Q}_w = \mathbf{N}_w^{-1}\mathbf{\Theta}^T(\mathbf{\Theta}\mathbf{N}_w^{-1}\mathbf{\Theta}^T + \mathbf{R}_{nn})^{-1}. \tag{3.28}$$

How the noise is modelled in this matrix depends on the noise correction methods applied. Several methods are discussed later in chapter 5.

Three ways to calculate the matrix $\mathbf{Q}$ through the characterization matrix $\mathbf{\Theta}$ have been shown of which two are applied in practice. In this case $\mathbf{\Theta}$ was calculated from experimental data previously obtained. Another direct method is *Hardeberg's modified pseudo inverse* [1, 4, 4]. In this method, prior statistical knowledge of the spectral reflectances of obtained objects is used to generate a suitable pseudo inverse. This is quite similar to the autocorrelation matrix $\mathbf{R}_{rr}$ used for Wiener's filter and therefore will not be discussed here in detail. Conceptually different to these are the learning based methods, although they require previous knowledge of spectral reflectances acquired through the system as well. These will be covered in the next section about *indirect methods*.

3.2.3 Indirect Methods

Leaving $\mathbf{\Theta}$ unknown, matrix $\mathbf{Q}$ has to be calculated in a different manner. This is achieved through learning. Values are obtained using calibrated color charts with p different color patches. For these patches sensor responses are acquired using the multispectral imaging system. The responses are included column-wise in a $n \times p$ camera response matrix $\mathbf{A}$ for n channels. Another $m \times p$ matrix $\mathbf{R}$ contains the corresponding spectral reflectances in its columns, which are sampled in m intervals. The spectral

reflectances are either previously known or obtained via a spectroradiometer under the same conditions as the sensor responses. From the patches the matrix $\mathbf{Q}$ is learned, thus these methods are called learning methods as well.

The problem to be solved can now be stated using equation 3.5 as:

$$\mathbf{R} = \mathbf{QA}. \tag{3.29}$$

In order to solve for $\mathbf{Q}$ this equation has to be adapted. Transposing it leaves:

$$\mathbf{R}^T = \mathbf{A}^T\mathbf{Q}^T. \tag{3.30}$$

For the i-th row $\mathbf{r}_i$ of $\mathbf{R}$ and the i-th row $\mathbf{a}_i$ of $\mathbf{A}$ the equation can be written:

$$\mathbf{r}_i^T = \mathbf{A}^T\mathbf{q}_i^T, \tag{3.31}$$

where $\mathbf{r}_i$ for $i = 1 \dots m$ and $\mathbf{A}$ are known and $\mathbf{q}$ has to be solved for. This is equivalent to the solution of the least square problem:

$$min\|\mathbf{A}^T\mathbf{q}_i^T - \mathbf{r}_i^T\|, \tag{3.32}$$

which has been discussed in section 3.2.1 and can be obtained using the pseudo inverse for overdetermined linear equation systems from equation 3.9:

$$\begin{aligned} \mathbf{q}_i^T &= (\mathbf{A}^T)^+_{over}\mathbf{r}_i^T \\ &= (\mathbf{A}^T\mathbf{A})^{-1}\mathbf{A}\mathbf{r}_i^T. \end{aligned} \tag{3.33}$$

Writing equation 3.33 again in matrix form for rows $\mathbf{q}_i^T$, with $i = 1 \dots m$, matrix $\mathbf{Q}^T$ becomes:

$$\mathbf{Q}^T = (\mathbf{A}^T\mathbf{A})^{-1}\mathbf{A}\mathbf{R}^T, \tag{3.34}$$

which lets us obtain matrix $\mathbf{Q}$ using the transpose:

$$\mathbf{Q} = \mathbf{R}\mathbf{A}^T(\mathbf{A}\mathbf{A}^T)^{-1}. \tag{3.35}$$

Equation 3.35 looks quite familiar compared to the direct method. Please note that although both approaches of reconstruction methods yield a similar pseudo inverse, direct and indirect methods are conceptually completely different. In the direct case

equation 3.16 derives from an underdetermined linear equation which minimizes the distance between the original spectral reflectance $\mathbf{r}$ and its approximation $\mathbf{r}'$. Matrix $\mathbf{Q}$ is then the pseudo inverse for the channel response matrix $\mathbf{\Theta}$ and can be calculated directly. $\mathbf{\Theta}$ is obtained by a series of experiments characterizing the system.

In the indirect case $\mathbf{\Theta}$ is unknown. Matrix $\mathbf{Q}$ is learned through a set of sample patches. Pairs of known spectral reflectances and the corresponding system responses are adapted. Then an overdetermined least square problem given in equation 3.32 is solved. The next sections will give further insight into learning based methods.

3.2.3.1 Sample Patches

The data for the learning methods are usually obtained via a color chart containing p single patches. From this data the spectral reflectance matrix $\mathbf{R}$ is built using a spectrometer. It contains a measurement for each patch in its columns. Further the patches are measured with the multispectral imaging system. The average sensor response of each patch goes into matrix $\mathbf{A}$ as column vector. Each column in $\mathbf{A}$ corresponds to a column in $\mathbf{R}$. From this data the pseudo inverse $\mathbf{Q}$ can be calculated. To receive adequate results with this method, the color chart should be a representative collection of surfaces, which can be expected to be present during following measurements.

Another approach on how to obtain the data takes noise into account. It was introduced by Imai, Taplin, and Day [32]. Non-averaged sample patches are used, containing all values of a sample patch in the matrix $\mathbf{A}$. Analogously, matrix $\mathbf{R}$ is extended by the spectral reflectances in its columns for every column of $\mathbf{A}$ corresponding to a point of the same color patch. This increases the matrix dimensions drastically. For instance for a color chart containing 200 patches matrix and using 10 channels, $\mathbf{R}$ has dimension 40×200 and matrix $\mathbf{A}$ 10×200. Using the non-averaged approach for a small window size of 10×10, the matrix columns are expanded by factor 100. Matrix $\mathbf{R}$ becomes of dimension $40 \times 20,000$ and matrix $\mathbf{A}$ $10 \times 20,000$. For even bigger window sizes, the computational times increase much more.

The advantage of the non-averaged approach is that every pixel can be assumed to be taken under a process including noise. This holds as long as the color patches are uniform and corrections for spatial inhomogeneities in illumination and CCD sensor are made. In this case all the calculations already take noise into account and therefore the model includes implicitly noise. Through this method noise does not have to be

explicitly modelled under theoretical assumptions.

3.2.3.2 Pseudo Inverse using PCA and SVD

As seen during the introduction of the pseudo inverse, one can use a least mean square approach to minimize the distance between a vector and its estimate. The inverse can also be stated in the sense of the *principle component analysis* (PCA). This method was introduced by Burns and Berns [33] and can be found in detail in Burns' PhD thesis [34].

PCA is defined as an orthogonal linear transformation that converts the data to a new coordinate system such that the first component, given through the first coordinate, has the highest variance. The following components have the highest variance under the constraint that they are orthogonal to the previous component. The total number of components is less than or equal to the number of original observations. In linear algebra PCA is calculated using *singular value decomposition* (SVD). The basic observations $\mathbf{X}$ are decomposed as following:

$$\mathbf{X} = \mathbf{U}\mathbf{\Sigma}\mathbf{V}^T, \tag{3.36}$$

where $\mathbf{U}$ is the matrix of eigenvectors of the coefficient matrix $\mathbf{X}\mathbf{X}^T$. Matrix $\mathbf{\Sigma}$ contains the singular values of $\mathbf{X}$ and $\mathbf{V}$ is the matrix of eigenvectors of the coefficient matrix $\mathbf{X}^T\mathbf{X}$. Having the mean centered SVD of a matrix $\mathbf{X}$, the PCA is defined as:

$$\mathbf{Y}\mathbf{U}^T\mathbf{X}. \tag{3.37}$$

This equation can be expressed using SVD of $\mathbf{X}$ and the orthogonality of $\mathbf{U}$:

$$\begin{aligned} \mathbf{Y} &= \mathbf{U}^T\mathbf{U}\mathbf{\Sigma}\mathbf{V}^T \\ &= \mathbf{\Sigma}\mathbf{V}^T. \end{aligned} \tag{3.38}$$

One may interpret the complete process as matrix $\mathbf{U}$ containing an orthogonal basis on its columns and $\mathbf{\Sigma}\mathbf{V}^T$ containing the projection of $\mathbf{X}$ on the the vector space spanned by $\mathbf{U}$.

As mentioned before several times in this chapter, spectra follow a smooth curve without sharp spikes. This leads to a strong correlation between neighboring values. The set of

observed spectral reflectances is matrix $\mathbf{R}$. This matrix can be rewritten using PCA as

$$\mathbf{R} = \mathbf{UY}. \tag{3.39}$$

Including this statement in equation 3.35 for the pseudo inverse and using equation 3.37 the pseudo inverse using PCA, respectively SVD, is obtained through

$$\begin{aligned} \mathbf{Q}_{PCA} &= \mathbf{UYA}^T(\mathbf{AA}^T)^{-1} \\ &= \mathbf{U\Sigma V}^T\mathbf{A}^T(\mathbf{AA}^T)^{-1}. \end{aligned} \tag{3.40}$$

By using PCA, it is theoretically possible to reduce the noise of the multispectral imaging system. Therefore, instead of using all the coefficient in $\mathbf{U}$ and $\mathbf{\Sigma V}^T$, reduced matrices are used. These contain only the l most significant coefficients. A $m \times l$ matrix $\mathbf{U}_l$ is attained, which includes solely the columns corresponding to the most significant coefficients. Using SVD, these are the first l rows. Analogously the $l \times m$ matrix $\mathbf{\Sigma}_l$ is built by keeping only the first l rows:

$$\mathbf{Q}_{PCA} = \mathbf{U}_l\mathbf{\Sigma}_l\mathbf{V}^T\mathbf{A}^T(\mathbf{AA}^T)^{-1}. \tag{3.41}$$

Furthermore, one has to choose an adequate quantity of representative singular values. In their original study the authors selected the number of 5 to represent a spectral reflectance curve [33]. Another study conducted by Imai et al. supports this initial approach, indicating that for 5 values the error starts to stabilize on a plateau [32]. However these numbers are not justified and seem to be chosen arbitrary. The exact number of singular values should be estimated during the calibration of the multispectral imaging system. For instance, Cortes calculated the optimal number for his system to be seven [6].

Another method to calculate the pseudo inverse indirectly will be elaborated on next. It is an approach to introduce regularization by the constraint that a spectral curve cannot be negative due to its nature. It is a good example of how regularization is applied to the learning based methods.

3.2.3.3 Non-Negative Least Squares (NNLS) Algorithm

Imai, Taplin, and Day introduced the *non-negative least squares* (NNLS) algorithm to find the inverse operator [32]. The algorithm was first proposed by Lawson and Hanson in their book [35]. It solves the following problem, which can be redefined in the sense of multispectral imaging:

$$min\|\mathbf{Ex} - \mathbf{f}\|, \text{ subject to } \mathbf{x} \geq 0, \tag{3.42}$$

where $\mathbf{E}$ is a $m \times n$ matrix, $\mathbf{f}$ a m-vector, and $\mathbf{x}$ is the n-vector solved for. This is a special case of the *linear least squares with linear inequality constraints* (LSI), which is stated as:

$$min\|\mathbf{Ex} - \mathbf{f}\|, \text{ subject to } \mathbf{Gx} \geq h, \tag{3.43}$$

where $\mathbf{G}$ is a $m \times n$ matrix and h an m-vector. In the present special case $\mathbf{G}$ is the identity and $\mathbf{h} = \mathbf{0}$. The ability to consider least square problems with linear inequality constraints allows to have several constraints on the solution. In spectral reconstruction terms this is non-negativity, since spectral curves are never below zero.

The solution of this problem can be characterized by the following theorem [35]:

Theorem 1 *(Kuhn-Tucker Conditions for the LSI Problem)*
An n-vector $\hat{\mathbf{x}}$ *is a solution for the NNLS Problem if and only if there exists an m-vector* $\hat{\mathbf{y}}$ *and a partitioning of the integers* $1 \ldots m$ *into subsets* E *and* S *such that*

$$\mathbf{G}^T\hat{\mathbf{y}} = \mathbf{E}^T(\mathbf{E}\hat{\mathbf{x}} - \mathbf{f}), \tag{3.44}$$

$$\hat{r}_i = 0 \text{ for } i \in E, \quad \hat{r}_i > 0 \text{ for } i \in S, \tag{3.45}$$

$$\hat{y}_i \geq 0 \text{ for } i \in E, \quad \text{and } \hat{y}_i = 0 \text{ for } i \in S, \tag{3.46}$$

where

$$\hat{\mathbf{r}} = \mathbf{G}\hat{\mathbf{x}} - \mathbf{h}. \tag{3.47}$$

Lawson and Hanson provide a good explanation, which will be quoted here to give insight into this rather complex theorem [35, p. 160]:

> Let $\mathbf{g}_i^T$ denote the i-th row vector of the constraints matrix $\mathbf{G}$. The i-th constraint $\mathbf{g}_i^T\mathbf{x} \geq \mathbf{h}_i$ defines a feasible half-space containing all the vectors

$\mathbf{x}$ that fulfil the constraint. The vector $\mathbf{g}_i$ is orthogonal (normal) to the bounding hyperplane of this half-space and is directed into the feasible half-space. The point $\hat{\mathbf{x}}$ is in the half-spaces induced by the index set S (S for slack) and on the boundary of the half-spaces indexed by E (E for equality).

The vector $\mathbf{p} = \mathbf{E}^T(\mathbf{E}\hat{\mathbf{x}} - \mathbf{f})$ is the gradient vector of $\varphi(\mathbf{x}) = \frac{1}{2}\|\mathbf{E}\mathbf{x} - \mathbf{f}\|^2$ at $\mathbf{x} = \hat{\mathbf{x}}$. Since $\hat{\mathbf{y}}_i = 0$ for $i \notin E$ equation 3.44 can be written as

$$\sum_{i \in E} \hat{y}_i(-\mathbf{g}_i) = -\mathbf{p}, \tag{3.48}$$

which states that the negative gradient vector of φ at $\hat{\mathbf{x}}$ as a non-negative ($\hat{y}_i \geq 0$) linear combination of outward-pointing normals ($-\mathbf{g}_i$) to the constraint hyperplanes on which $\hat{\mathbf{x}}$ lies ($i \in E$). Geometrically this means that the negative gradient vector $-\mathbf{p}$ lies in the convex cone based at the point $\hat{\mathbf{x}}$ and is generated by the outward-pointing normals $-\mathbf{g}_i$.

Any perturbation $\mathbf{u}$ of $\hat{\mathbf{x}}$, such that $\hat{\mathbf{x}} + \mathbf{u}$ remains feasible, must satisfy $\mathbf{u}^T\mathbf{g}_i \geq 0$ for all $i \in E$. Through multiplying both sides of equation 3.48 by such a vector $\mathbf{u}^T$ and using the fact that $\hat{y}_i \geq 0$, it follows that $\mathbf{u}$ also satisfies $\mathbf{u}^T\mathbf{p} \geq 0$. From the identity $\varphi(\hat{\mathbf{x}} + \mathbf{u}) = \varphi(\hat{\mathbf{x}}) + \mathbf{u}^T\mathbf{p} + \|\mathbf{E}\mathbf{u}\|^2/2$, it ensues that no feasible perturbation of $\hat{\mathbf{x}}$ can reduce the value of φ.

Adapting the NNLS algorithm for the purposes in hand, one may state equation 3.42 as in equation 3.32:

$$min\|\mathbf{A}^T\mathbf{q}_i^T - \mathbf{r}_i^T\|, \tag{3.49}$$

where $\mathbf{A}$ is the sensor response matrix, $\mathbf{r}_i$ is the i-th row of the the matrix $\mathbf{R}$ containing the spectral reflectances, and $\mathbf{q}_i$ is the i-th row of the crucial operator $\mathbf{Q}$. Solving the problems for $i = 1 \ldots m$ results in the overall inverse operator $\mathbf{Q}_{NNLS}$. The adapted NNLS algorithm is given in algorithm 1.

As soon as the algorithm terminates, the solution vector $\mathbf{x}$ ($= \mathbf{q}_i^T$) satisfies

$$x_j > 0 \text{ for } j \in P, \text{ and } x_j = 0 \text{ for } j \in Z. \tag{3.50}$$

Analogously, the dual vector $\mathbf{w}$ satisfies

$$w_j = 0 \text{ for } j \in P, \quad x_j \leq 0 \text{ for } j \in Z, \tag{3.51}$$

Algorithm 1: NNLS Algorithm

Data: $\mathbf{A}^T$, $\mathbf{r}^T$
Result: $\mathbf{q}_i^T = \mathbf{x}$

$n \leftarrow$ number of columns in $\mathbf{A}^T$
$P \leftarrow \emptyset$, $Z \leftarrow \{1, \ldots, n\}$, $\mathbf{x} \leftarrow \mathbf{0}$
$\mathbf{w} \leftarrow \mathbf{A}(\mathbf{r}_i^T - \mathbf{A}^T\mathbf{x})$
while $Z \neq \emptyset \wedge$ *for* $j \in Z$ $\exists w_j > 0$ **do**
    find $t \in Z : \ w_t = max\{w_j | j \in Z\}$
    $P = P \setminus \{t\}$, $Z = Z \cup \{t\}$
    let the j-th column of matrix $\mathbf{A}_P$ be defined as:
    $\mathbf{a}_{P,j} := \begin{cases} j\text{-th column } \mathbf{a}_j \text{ of } \mathbf{A}^T, & \text{if } j \in P \\ \mathbf{0}, & \text{if } j \in Z \end{cases}$
    $\mathbf{z} \leftarrow$ solution of least squares problem $min\|\mathbf{A}_P\mathbf{z} - \mathbf{r}_i^T\|$
    while $\forall j \in P \ \exists z_j \leq 0$ **do**
        find $q \in P$ such that $\frac{x_q}{x_q - z_q} = min\{\frac{x_j}{x_j - z_j} | z_j \leq 0, \ j \in P\}$
        $\mathbf{x} \leftarrow \mathbf{x} + \frac{x_q}{x_q - z_q}(\mathbf{z} - \mathbf{x})$
        $\forall j \in P : x_j = 0$ **do** $P = P \setminus \{j\}$, $Z = Z \cup \{j\}$
        $\mathbf{z} \leftarrow$ **solution of least squares problem** $min\|\mathbf{A}_P\mathbf{z} - \mathbf{r}_i^T\|$
    $\mathbf{x} \leftarrow \mathbf{z}$
    $\mathbf{w} \leftarrow \mathbf{A}(\mathbf{r}_i^T - \mathbf{A}^T\mathbf{x})$

and

$$\mathbf{w} = \mathbf{A}(\mathbf{r}_i^T - \mathbf{A}^T\mathbf{x}). \tag{3.52}$$

Equation 3.50, 3.51, and 3.52 constitute the Kuhn-Tucker conditions for the NNLS problem. In consequence, the vector $\mathbf{x}$ ($= \mathbf{q}_i^T$) is the solution vector to the initial problem given in equation 3.42, respectively equation 3.49.

3.2.4 Interpolation Methods

For interpolation methods, the multispectral imaging system is assumed to sample spectral reflectance curves [6, 28]. In this case the spectral transmittance functions of filters are the sampling functions. Through direct interpolation of the camera response, the shape of the spectral curve is estimated. As an example, figure 3.3 shows the spectral curve of an object as well as the camera responses on the left and the linear interpolation of the camera responses on the right.

To achieve adequate results with interpolation, two prior characteristics of system have to be known. First the position of the measurements points. If the filter transmittance

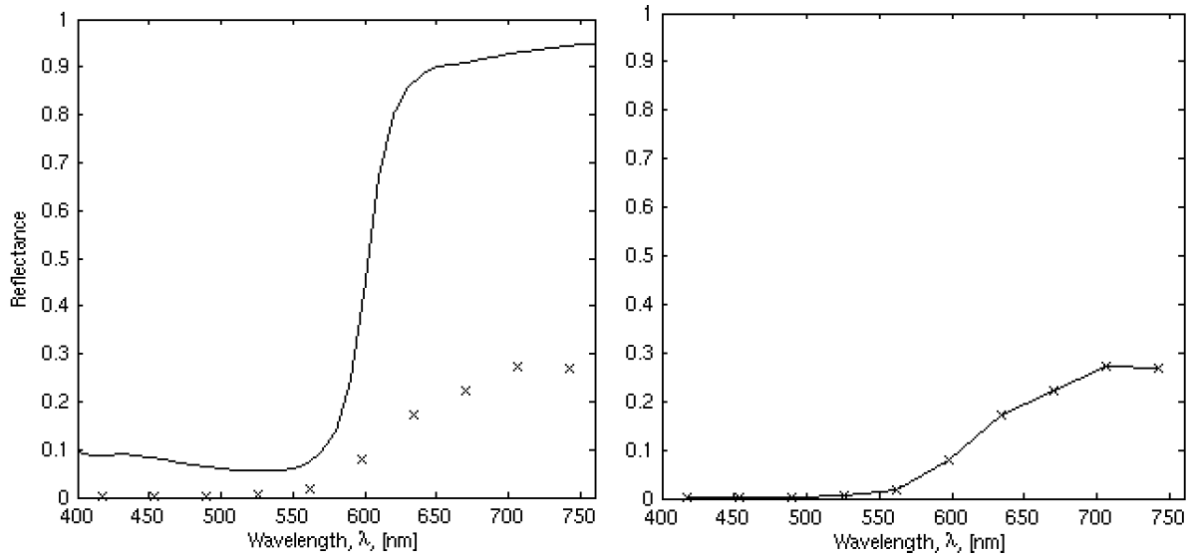

Figure 3.3: Spectral curve and camera responses [6].

is very narrow and Gaussian shaped, the peak of the curve can be assumed to be the measurements point, since the Gaussian functions of the filter are the basic sampling functions. For this reason only narrow-band filters can be used in the multispectral imaging system, if interpolation is used for the spectral reconstruction. More on the topic of narrow- and wide-band filters is discussed in the next chapter, see section 6.1.2.

Secondly, the camera response has to be normalized to the interval $]0, 1[$ for every channel. Furthermore, the actual spectral sensitivity of the channels has to be known. The normalization matrix can be obtained by experiment. An image of a perfect white under an illuminant is taken for every channel. The spectral radiance of the illuminant is of no matter, since the data is scaled to unity. It is however important that the sensor is illuminated equally diffuse. From this information the normalization matrix is adapted. If normalization is not performed, the resulting values will be poorly scaled and interpolation methods will produce wrong results. Figure 3.4 shows the camera response alongside the spectral curve without normalization on the left and linear interpolation of camera responses on the right. Through wrong scaling of the response values interpolation fails.

There exist several interpolation methods. Out of these, mostly two are used, *spline interpolation* and *modified discrete sine transformation* (MDST). Spline interpolation uses a special type of a piecewise polynomial interpolant called a spline. MDST is based on *discrete Fourier transformation* (DFT). The orthogonal basis derived during DFT

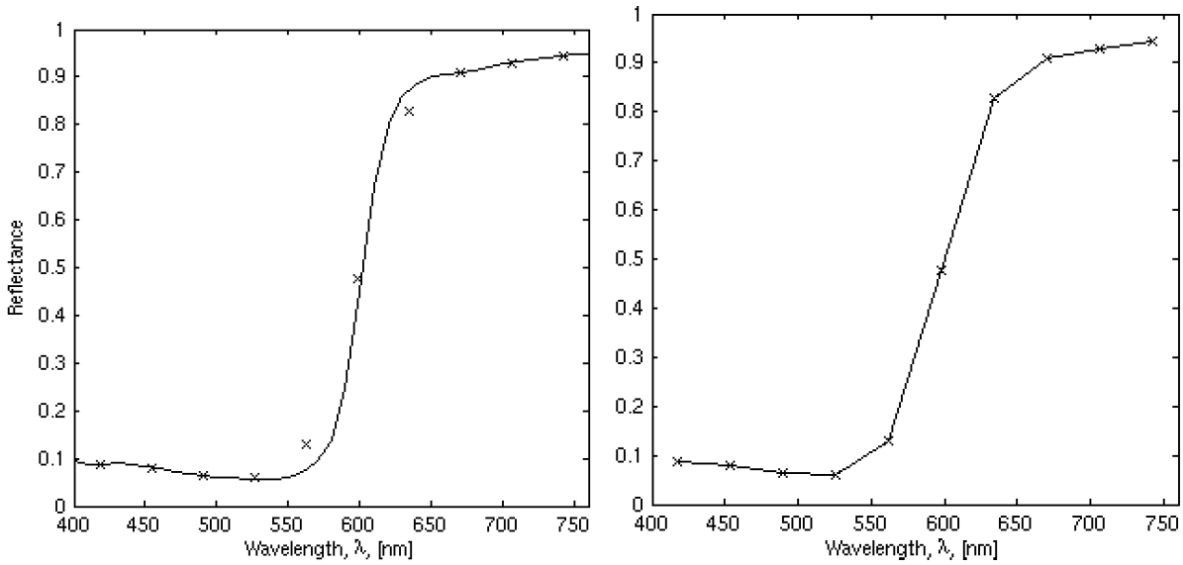

Figure 3.4: Spectral curve and camera responses without normalisation [6].

is used as interpolation function. Both methods are very complex and go beyond the scope of this thesis[1].

3.3 Conclusion

At the beginning of the chapter the system model of a multispectral imaging system was introduced. This model depends on the illuminant and observed object, as well as on the intrinsic camera attributes. Based on this model it was shown how the spectral reflectance estimation can be derived. There are many different spectral reconstruction methods which are based on this estimation. They can be categorized in direct, indirect or interpolation methods.

The quality of the spectral reflectance estimation methods depends greatly on the purpose of the system. If prior information of the spectral reflectance of objects, respectively scenes, is available, it can be used for learning-based methods. In this case, interpolation or direct methods are outperformed. For a more general application, e.g. the recording of natural scenes, direct methods and interpolation are superior. In theory, direct methods should produce more accurate results than interpolation. In practice, noise occurs and the calibration process is very complex. This argues in favor of interpolation, since,

[1]The interested reader can find further information in [36, 37].

beside the normalisation matrix, the calibration process is rather simple and therefore the calibration error is small.

The next chapter introduces the hardware required to build and calibrate a multispectral imaging system. Hardware and models are strongly correlated, since the model depends on the purpose of the system, as does the selection of the devices.

Chapter 4

System and Secondary Devices

Contents

Currently, only few implementations of multispectral imaging systems exist. If they do not acquire images through direct measurements using a radiometer, they mostly use a monochrome CCD camera combined with a filter. This chapter discusses the device setup for multispectral imaging systems. The setup presented here is the state of the art and widely used for multispectral imaging, as they were encountered in nearly all the publications evaluated, for example [1, 6, 15, 28, 38]. Further specialised hardware is required for precise calibration of the system. These contain light sources, spectrometers, and color charts which are used for different spectral reconstruction methods.

4.1 System Devices

Since post processing steps are required to estimate the actual spectra, the images are recorded digitally. For this purpose monochrome CCD cameras are used. As ever, the more sophisticated the hardware, the more expensive it is. General CCD sensors used in consumer electronics are cheap and widely spread. However they have various disadvantages. Amongst others, the CCD sensors of commercial cameras contain large numbers of defects and blemishes. To cope with these effects, the camera software post processes the images. However, this introduces inaccuracies to the picture. For scientific use, its quality is then inacceptably degraded. Images recorded with sophisticated hardware still contain noise, nevertheless it is largely reduced compared to regular devices. Detailed knowledge about CCDs helps to cope for inaccuracies, for example read out noise discussed in the next chapter.

Alongside to the camera, a lens of some kind is required. The lens is selected by the needs of the later recorded scenes, i.e. landscapes, paintings, etc. The influence of lenses on images is discussed in detail in section 4.1.2 when elaborating on the different techniques used for filters.

4.1.1 Charge Coupled Device (CCDs) Cameras

Charge coupled devices (CCDs) were invented by Willard Boyle and George Smith in 1970 at the AT&T Bell Labs [39]. Originally they were built as storage structures, but it was soon discovered that they are sensitive to light and make it very easy to record a 2D image. For the invention of CCDs Boyle and Smith received the Nobel Prize for Physics in 2009. A CCD is a semiconductor architecture in which charge is transferred through storage areas. The CCD is divided into small light-sensitive areas, the pixels. Through these pixels one is able to record a scene. The number of electrons collected at each pixel is directly proportional to the light intensity of the scene. Figure 4.1 shows a close up photograph of a CCD mounted on a board. A CCD is primarily made of silicon that has an altered structure. Some of the silicon atoms have been replaced with impurity atoms.

Figure 4.2 shows a profile of a CCD. One notices that the silicon is not made of individual pixels. These are defined by the electrodes above the CCD. The simplified workflow is described as follows: If a photon hits a silicon atom near a CCD photodiode, a electron-

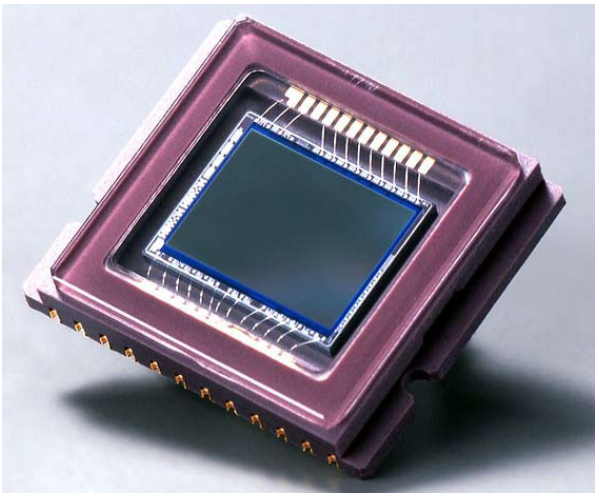

Figure 4.1: Close up of a charge coupled device [40].

hole pair is created. The electron is then separated through the diode. Furthermore, all positively charged holes will be repelled from the area around the electrode. Under this circumstances a potential well is formed which is located deep within the silicon. In it all the electrons produced by incoming photons are collected.

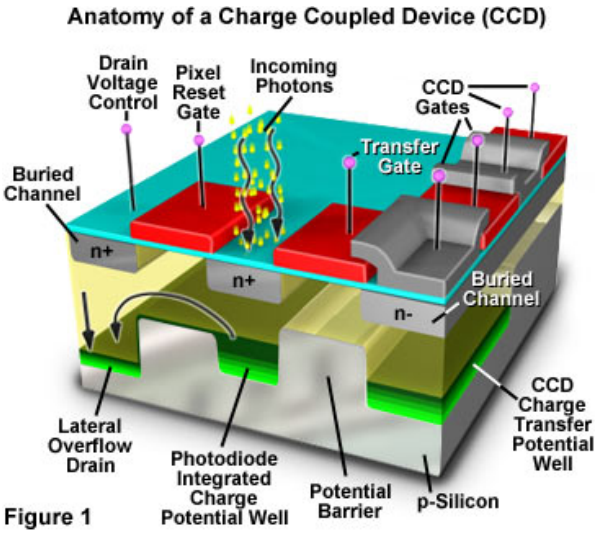

Figure 4.2: The profile of a CCD [41].

The longer the CCD is exposed to light, the more electrons are collected in the potential wells that are associated with the electrodes. The full well capacity provides the amount of electrons that can be stored under a pixel. After a pixel was exposed to a scene for a given period, the accumulated photo-electrons are converted to a voltage signal in proportion to their number. This signal is then amplified by an amount proportional

to the *ISO gain*, shortly referred to as ISO, set in the camera. Eventually, it has to be translated to a digital signal by an *analog-to-digital converter* ADC. For each pixel there is a digital number representing the photons counted. The signals for all pixels combined supply the raw image pixel values.

The shutter is opened for the exposure time and the potential wells are filled with electrons. If a potential well is full before the exposure time ends, a pixel is over-exposed. This results in further information being lost. To prevent this effect, a proper exposure time corresponding to the intensity of the light in the scene has to be chosen. After a scene has been recorded, the shutter is closed to prevent more photons to impact the CCD. Before the next scene can be recorded the potential wells have to be emptied.

The CCD itself consists of many pixels, respectively potential wells, arranged in rows and columns. The resolution of the CCD is defined by the size of the pixels, as well as by their separation, called pitch. Figure 4.3 indicates this setup. One can see the strong correlation between the CCD and the later digital image which will have the same form.

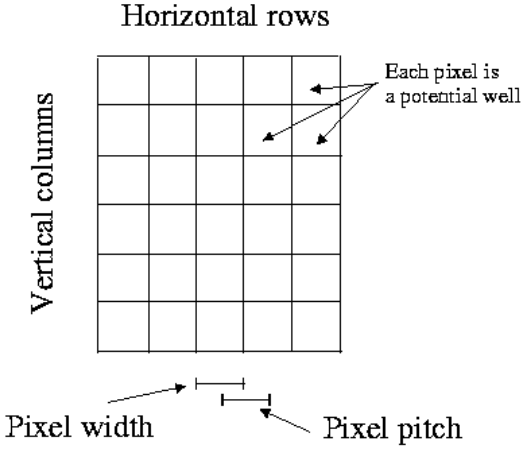

Figure 4.3: Horizontal and vertical structure of a CCD [42].

4.1.2 Filter

There are two different techniques used when connecting filters to the lens of a camera. The first one is by selecting individual filters mounting them on a filter wheel, as it is done in [9]. The second one is by using a tunable liquid crystal filter, as presented in [2]. As mentioned in the last chapter, review section 3.1 and equation 3.3, the camera model building the basis for the spectral reconstruction requires uniform sampling at equal

wavelength intervals. This restricts which filters can actually be used for a multispectral imaging system.

Filters are defined by their spectral transmittance. This means that filters only allow a certain amount of the light to bypass it over a given spectrum. The spectral transmittance further divides filters in narrow- and wide-band. Narrow-band filters simplify the estimations of spectral reflectances, since they produce small Gaussian shaped curves with easy to identify single peaks. This improves the precision of the individual channels. Typically filters are selected in an interval from 400 nm to 720 nm which covers the biggest and most dominant part of the spectrum of light visible to the human eye.

When selecting filters for a filter wheel, one has to keep in mind that the number and their transmittance heavily impact the quality of the multispectral imaging system. The optimal choice is given when the selected filters maximize the orthogonality of the camera channels when applying them to reflectances that are highly representative of the statistical spectral properties of the objects that are to be imaged in a particular application. This does not necessarily mean that a multispectral imaging system using a selection of filters has to be very narrow in its usage, for example just to archive pictures in a museum. It simply allows to reduce the number of required filters for these scenarios and to improve the quality of the spectral reconstruction for more sophisticated purposes.

In order to search for the right filters, Hardeberg proposed a sequential selection of the filters to maximize their degree of orthogonality after projection into the vector space spanned by the most significant reflectance eigenvectors [4]. Although this approach is not optimal, this method is much less time consuming and cost efficient than examining many single filters in detail. Figure 4.4 illustrates the process for a selection of seven filters from a set of 37 Kodak Wratten, Hoffman, and Schott filters. The numbering indicates the order of selection. Additionally, one can detect an example for a narrow-band in the blue curve, while the pink curve represents a wide-band filter.

A liquid crystal tunable filter is different to a selection of single filters [43, 2]. It is merely one filter that can alter its transmittance by electronically controlled liquid crystals. There are many different designs of these filers with various working principles [44]. Such a filter has many advantages over a set of individual filters.

Firstly, no evaluations of single filters has to be done in order to find the best matching collection. The tunable filter can be stepped through smoothly over the interval of

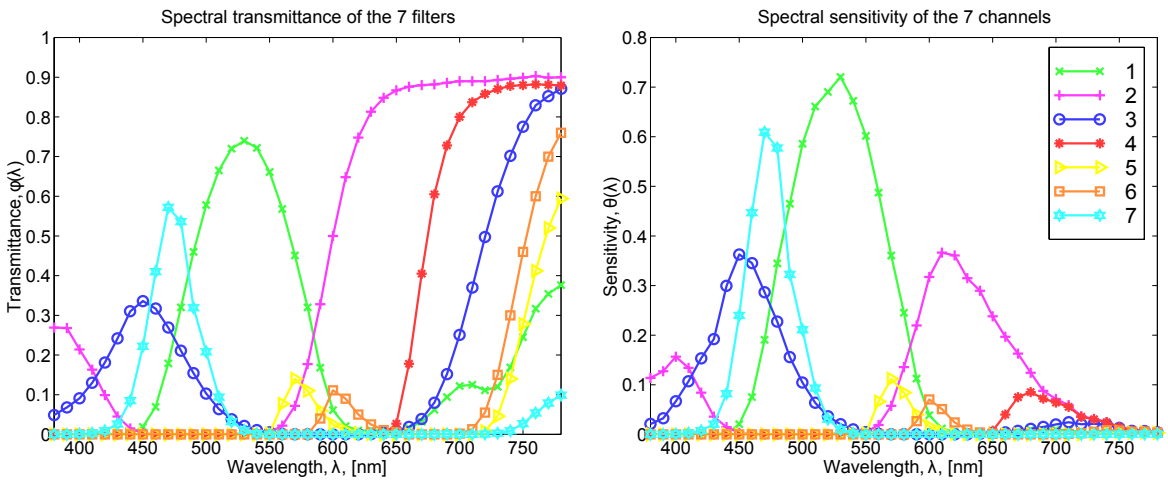

Figure 4.4: Sequential selection of filters as proposed by Hadreberg [4].

interest. The design of the filter allows the individual channel-curves to be very narrow and Gaussian-like shaped. This means that the channels can be freely selected and only overlap in small areas, see figure 4.5. Furthermore, individual filters have distinct effects besides transmittance, e.g. vignetting or aberrations, which have to be compensated for during calibration. This only has to be done just once for a tunable filter. Finally, the whole mechanical setup of the multispectral imaging becomes easier, since there is no additional filter wheel required.

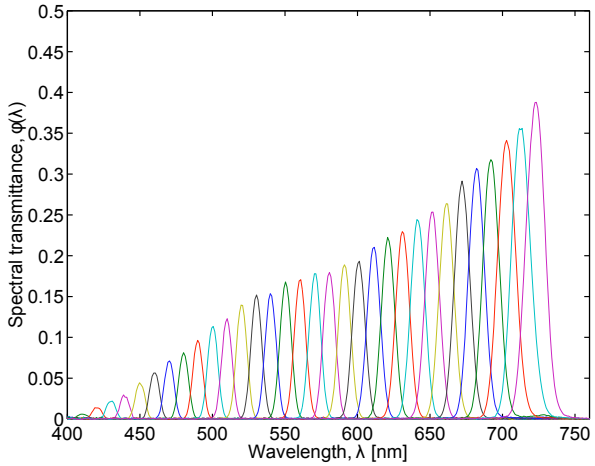

Figure 4.5: Spectral transmittance of a VariSpec from Cambridge Research & Instrumentation (CRI) at a selection of different channels [2].

The only actual disadvantage of a tunable filter over a collection of filters are the channels located at small wavelengths around 400 nm to 420 nm. The spectral transmittance of these channels is very small, which makes the recorded images fragile to noise. Fur-

thermore, the shape of the curves is not Gaussian like anymore, but instead contains spikes and edges. This leads to more effort during the calibration process as well as to inaccuracies for the small channels in the recorded images.

4.2 Secondary Devices

Secondary devices are required for calibration and validation of the multispectral imaging system. There are two experimental setups correlating to the direct or indirect spectral reconstruction methods presented in section 3.2.

For the direct method, a monochromator is used together with an integrated sphere. A monochromator is an optical device which allows the isolation of a specific wavelength of an incoming electromagnetic radiation. Originally the radiation is polychromatic, meaning it consists of different wavelengths. The monochromator uses a prism or a grating to separate the different wavelengths and absorbs or diffracts the unspecified part. Figure 4.6 shows the working principle of a Czerny-Turner monochromator. Light (A) falls through an entry slit (B) onto a curved mirror (C). The collimated (focused at infinity) light is diffracted from the grating (D) and collected by another mirror (E), which refocuses the dispersed light on the exit slit (F). Although in detail there are different architectures used in different monochromators, the underlying principle is always the same.

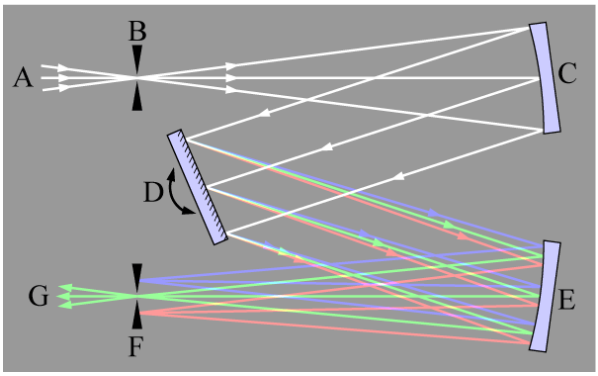

Figure 4.6: Diagram of a Czerny-Turner monochromator [45].

To cause the light homogeneously cover the whole viewing field of the camera, an integrated sphere is required. An integrated sphere is a hollow sphere that in its inside diffusely reflects incoming light. Through a hole that lies in a right angle to the light

source, the light can be measured. The inner part of the sphere is coated with barium sulfate ($BaSO_4$), which has good reflection properties. This setup is more sophisticated than using merely a color chart. It allows a higher precision, since the light is diffuse and, as long as the devices are properly used, no stray light enters the system. Figure 4.7 gives a profile of an integrated sphere.

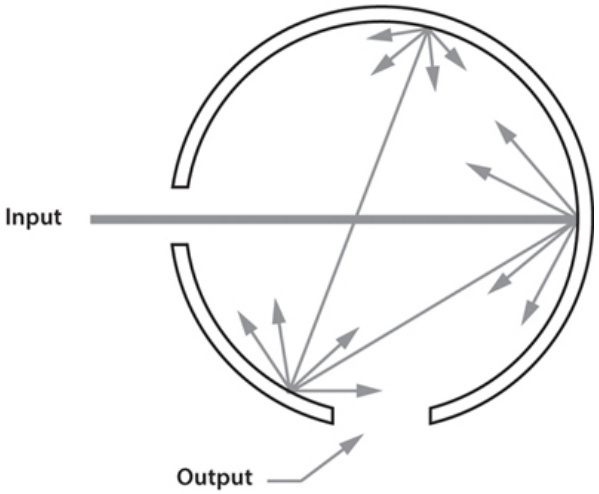

Figure 4.7: Diagram of an integrated sphere [46].

The method previously presented allows the building of the channel response $\mathbf{\Theta}$ required for calculating the inverse $\mathbf{Q}$ in the direct spectral reconstruction, presented in section 3.2.2. The response of the camera for the different channels can be recorded for any given interval by stepping through the wavelengths via the monochromator.

Although the same devices could be used for the indirect methods shown in 3.2.3, in practice color charts together with a simple illuminant are easier to handle and of much lower price. The illuminant should be as stable as possible and deliver an equal illumination of the chart. A color chart contains an arrangement of standardized colors. For good calibration results, the color chart should contain around 160–240 color patches [6]. Figure 4.8 gives an example for an adequate color chart containing 240 colors.

The channel response $\mathbf{A}$ can be measured through color charts. In both methods the real spectra $\mathbf{R}$ are required. In the indirect case $\mathbf{R}$ is used for the calculations in 3.35. In the direct case it is used to normalize the channel response against the actual intensity of the measured light.

The real spectra are measured through the usage of a spectrometer. A spectrometer is a device to measure properties of light over a specific portion of the electromagnetic

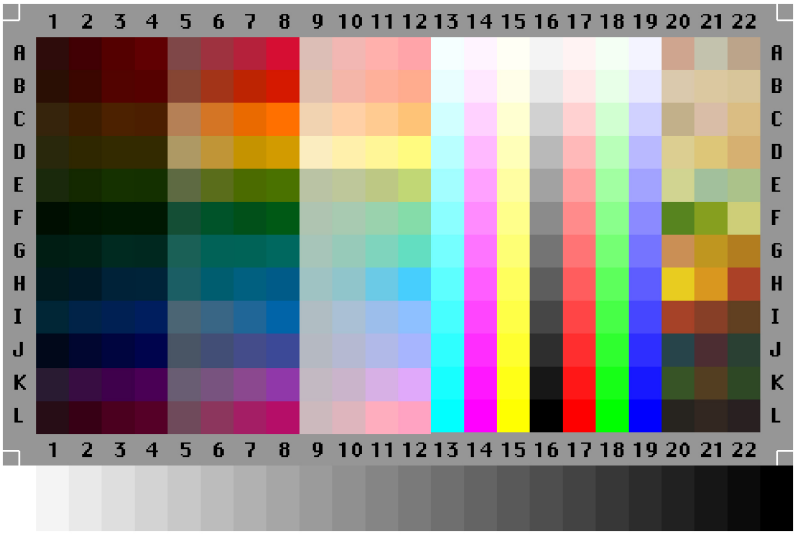

Figure 4.8: An IT8.7 target color chart by LaserSoft Imaging [47].

spectrum. The working principle is the same as for a monochromator combined with a detector. The difference of the wavelengths of the incoming light is analyzed either by refracting the light through a prism or by diffracting it by a grating, as well as measuring the frequencies in an interferometer via a Fourier analysis. While a spectrometer only provides the spectrum of one specific area of the scene, a calibrated multispectral imaging system is a spectral photometer, measuring the spectrum of a whole scene.

4.3 Conclusion

Several devices used to build and calibrate a multispectral system have been introduced in this chapter. The system itself consists of a CCD camera, a lens and a series of filters or one tunable filter. For calibration, either a monochromator and an integrated sphere or color charts and an illuminant is required. Which setup is used depends on the spectral reconstruction method and, hence, on the purpose of the system. However, through flaws in the architecture, respectively the devices themselves, small errors in the images arise. How to cope with this noise will be discussed in the next chapter.

Chapter 5

Noise Correction

Contents

As seen in the previous chapter, a multispectral imaging system consists of various devices. These devices introduce several sources of noise. For example the CCD sensor response is not equal at every pixel. Others happen due to the nature of the used optics in form of the sensor, in our case filter and lens. For this reason the output signal of the multispectral imaging system has to be corrected. In this chapter noise common in multispectral imaging systems is presented. Further, several methods are shown to cope for the imaging errors introduced by noise. All noise correction methods together build the *flat field* noise correction algorithm. The information presented in this chapter is based on [48, 49, 50].

5.1 Read Out Noise

In section 4.1.1 the functional principle of a CCD was described. Photon-electrons are collected for the duration of the exposure. They are converted to a voltage signal proportional to the count. This signal is amplified by the ISO and finally an ADC translates it to a digital signal. This provides the raw image pixel values.

In the ideal case, the raw image pixel values would be directly proportional to the photon count. This factor indicating proportionality is a constant scale factor and is called the gain of the sensor. However, it is not a gain in the literal sense, since it is a conversion factor between the counted photo-electrons and the raw image pixel values. Doubling the ISO reduplicates the raw value for a preset exposure. However, the same number of captured photons is converted into a raw value twice as big. This means that doubling the ISO halves the gain. Therefore the gain is inversely proportional to the ISO.

For real measurements, the raw values do not precisely reflect the counted photons. Each step — from sensel readout, to ISO gain, to digitization—in the conversion from the original count to the raw value suffers voltage fluctuations. These contribute to a deviation of the raw value from the ideal value proportional to the photon count. In the raw values they constitute the read out noise of the sensor due to the signal processing electronics.

One part of the read noise can be measured by taking the bias frame. Here, the exposure is set to the shortest time possible by the device. The lens cap is on, the shutter closed and the image is preferably taken in a dark room. In this case there are no photons captured, and only the electronic noise from reading the sensor remains for every pixel. This value can then be subtracted from subsequently recorded images, reducing the recording error due to electronic gain. Each given image p is modified by the bias image b through by the following equation:

$$q = p - b, \tag{5.1}$$

where q is the image under noise correction.

Beside the constant factor there exists a fluctuating component of the read out noise. This undesired property can be removed by taking an average over a set of consecutive frames. Depending on the quality of the camera, it requires a series of 30 to 100 images to compensate. In practice this might be difficult as the exposure times might be very

long or the scene includes moving objects. However, it should be done whenever possible. It can be included taking the mean of n images of the same scene:

$$q = \frac{1}{n}(\sum_{i=1}^{n} p_i) - b. \tag{5.2}$$

5.2 Dark Current Noise

Dark current is the relatively small electric current that flows through CCDs even when no photons are entering the device. In contrast to the ambient read out noise, it grows with the exposure time. Dark current arises from thermal energy within the silicon lattice comprising the CCD. Therefore dark current is sometimes referred to as thermal noise. Electrons are created over time, being independent of the light falling on the sensor. This effect is amplified if the CCD gets warmer. Thermal electrons are freed at a relatively constant rate per unit time, thus thermal noise increases with exposure time. These electrons are captured by the CCD and counted as signal.

The effect of dark current in a multispectral imaging system can be measured by taking images with the lens cap on and the shutter closed in a dark room. The images are taken in sequence and under different exposures in order to reduce the uncertainty of read out noise and to see its influence. Finally the bias frame is subtracted from the dark current images to remove the effect of read out noise. To remove the effect of dark current this artificial image can be scaled by a factor which is depending on the exposure time and added to the bias. This leads to the following equation:

$$q = \frac{1}{n}(\sum_{i=1}^{n} p_i) - b - s_e d, \tag{5.3}$$

where d is the dark current frame and s_e the exposure scale factor.

This approach has the advantage to address another source of noise. Particular pixels of the CCD are susceptible to giving brighter intensities above the general background noise. This effect gets noticeable during longer exposure shots and is called fixed pattern noise. Even though fixed pattern noise is just a small contributor to noise, it is quite apparent because our perception is adapted to picking out patterns, see figure 5.1 where a grid like pattern is standing out.

Dark current is heavily dependent on thermal factors. In order to further reduce the

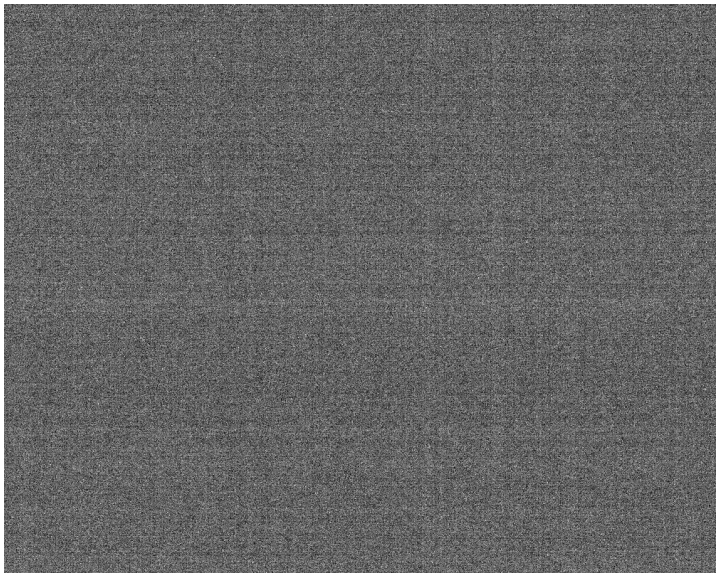

Figure 5.1: An example of fixed pattern noise [51].

effect of dark current on images, CCDs can be chilled either with thermoelectric coolers or liquid nitrogen. Ideally, the dark current noise should be reduced to a point where its contribution is negligible over a typical exposure time.

5.3 Vignetting

Vignetting is effect dependant on the optics of the system. For multispectral imaging systems these are the filter and the lens. The effect reduces the brightness and saturation in the periphery of the image compared to its center. Figure 5.2 gives a clear but exaggerated impression of the impact of an image. The effect was produced by altering the focal length, left to right 8 mm, 10 mm, 12 mm, 14 mm, and 16 mm, of a APS-C digital SLR camera and an aperture of $f/4.5 - 5.6$ DC HSM lens with its friction fit sleeve ring attached.

There are several types of vignetting. For multispectral imaging system two of these are relevant. The first one is mechanical vignetting and occurs when light beams emanating from object points located off-axis are partially blocked by external objects. In the case of a multispectral imaging system this is the filter. The effect on the image is the changing of the entrance pupil shape as a function of angle. The darkening can be gradual or abrupt, depending on the lens aperture. The smaller the aperture, the more abrupt the vignetting as a function of angle. Complete blackening is possible with

Figure 5.2: Visual effect of vignetting [52].

mechanical vignetting, when the corner of the image is essentially imaging the inside of the lens hood or filter holder. The second one is optical vignetting and is caused by the physical dimensions of a multiple element lens. Rear elements are shaded by elements in front of them, which reduces the effective lens opening for off-axis incident light. The result is a gradual decrease in light intensity towards the image periphery.

The effect of vignetting can be removed by taking a reference image under homogeneous light. This image is corrected for bias and dark current. Every image recorded by the system with the same optics, respectively lens and filter, can then in turn be corrected by dividing through this reference image. Since the effect of vignetting depends on focal length and aperture, for every pair of settings a reference image has to be taken. Together with equation 5.3 this leaves for the noise-corrected image:

$$q = \frac{\frac{1}{n}(\sum_{i=1}^{n} p_i) - b - s_e d}{v_{f,m}}, \tag{5.4}$$

where $v_{f,m}$ is the vignetting reference image, f the focal length and m the aperture. This is also the final algorithm for flat field noise correction.

5.4 Conclusion

Several sources of noise and their effects were shown in this chapter. Although the noise can never be removed completely, there are many methods to greatly reduce it. However, these methods might seem easy in theory, but require effort in practice. This is due to the fact that the reference images, bias, dark current frame, and vignetting images have to be recorded during camera calibration. Nevertheless experiments have shown that it

is worth the effort, which was motivation to be used in my own work. Beginning with the next chapter my own experimental work will be introduced. I start by describing the devices used for our multispectral imaging system and their properties.

Chapter 6

Implementation of a Multispectral Imaging System

Contents

After explaining the theory behind multispectral image acquisition in detail, I now introduce our own multispectral imaging system. This chapter is about the specifications of the devices that were integrated into the system or used for calibration. Furthermore, the common software framework which allows a joint usage of the devices is briefly described. All devices belong to the *Institute for Optical Systems* (IOS), the workgroup of Prof. Dr. Mathias Franz at the HTWG Konstanz. We built the system in cooperation with his workgroup.

6.1 Hardware

First, the devices used in the multispectral imaging system will be shown. We gathered our first experiences in multispectral imaging with a PCO.Camera 4000. However, for various reason that will be explained in the next section, we replaced this camera by an AVT Bigeye G132. This camera together with a Computar M7528-MP as lens and a CRI VariSpec as filter builds our multispectral imaging system. The devices used for calibration will be discussed after the introduction of the parts integrated in the system.

6.1.1 CCD Camera

The first camera we used was a *PCO.Camera 4000* [53] of the manufacturer *PCO.Imaging*. The device is equipped with a monochrome CCD. The output depth is 14bit and the sensor has a high resolution of 4008×2672 pixels. Through thermoelectric cooling, which allows a difference of $-45°$C versus ambient temperature, as well as through sophisticated electric design, the overall noise is kept relatively small. The image data is transferred by a FireWire serial data bus. The exposure range of the camera lies between 5μs and 60s. Figure 6.1 displays an image of the camera.

Figure 6.1: PCO camera 4000 [53].

After initial testing we replaced the PCO.Camera 4000 by an *Allied Vision Technologies* (AVT) *Bigeye G-132B camera* [54]. This is a peltier cooled CCD camera with a Sony ICX285 CCD. The output depth of the sensor is 12bit and it has a resolution of 1280×1024 pixels. The sensor is cooled to $-20°$C. As lens a Computar M7528-MP was used [55]. It has a maximal focal length f of 75mm and a maximal aperture ratio of f/2.8. Figure 6.2 shows an image of the camera.

Figure 6.2: AVT Bigeye G132 [54].

There have been several reasons for replacing the PCO.Camera 4000 through the AVT Bigeye G-132B, notwithstanding the former has a higher resolution and output depth. In the first place, the latter camera achieves even less noise. Secondly, its exposure time lies in a range from 81ms up to 4292s which is roughly 71min. This allows a more proper calibration at small wavelengths due to the monochromator producing smaller intensities. Third, the camera has a larger quantum efficiency which is mostly relevant for recording at small wavelengths, since the filter transmittance at these values is very small (compare to figure 6.4). In figure 6.3 the absolute quantum efficiencies of the two cameras are plotted next to each other. On the left side one can see that the quantum efficiency for the PCO.Camera 4000 is smaller in average compared to the one of the Bigeye G-132B on the right.

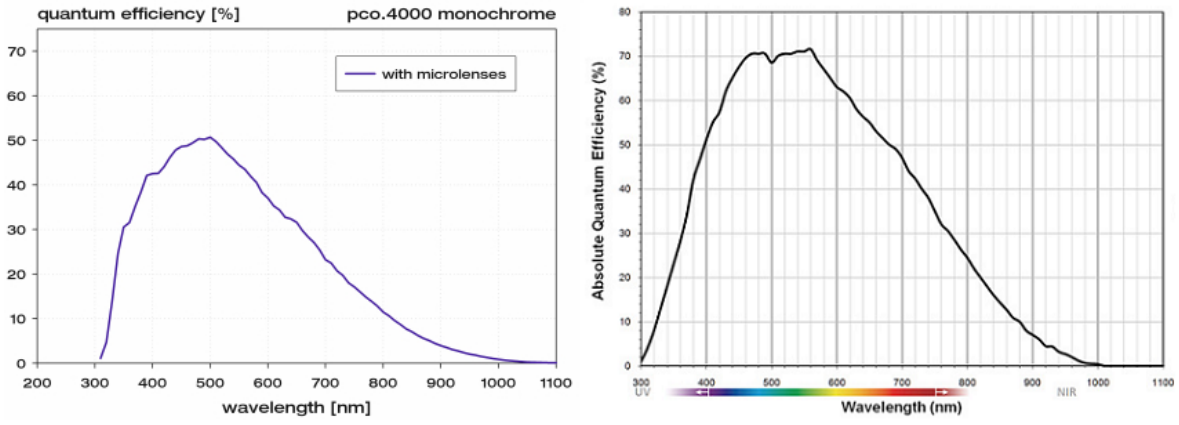

Figure 6.3: PCO camera 4000 (left) and AVT Bigeye G-132B (right) quantum efficiency as given by the manufacturers [53, 54].

6.1.2 Tunable Filter

Instead of a collection of filters, we used a *CRI VariSpec Liquid Crystal Tunable Filter (LCTF)* [56]. We preferred this approach because it is easier to handle mechanically and the filter is very narrow. This allows precise measurements and the usage of interpolation methods for the spectral reconstruction. The filter is connected and controlled by USB. Figure 6.4 shows a plot of the filter transmittance for a selection of 33 channels between 395nm and 750nm. It can be observed that the filter transmittance at the left border of the wavelengths, for example at a wavelengths of 400nm, is very small.

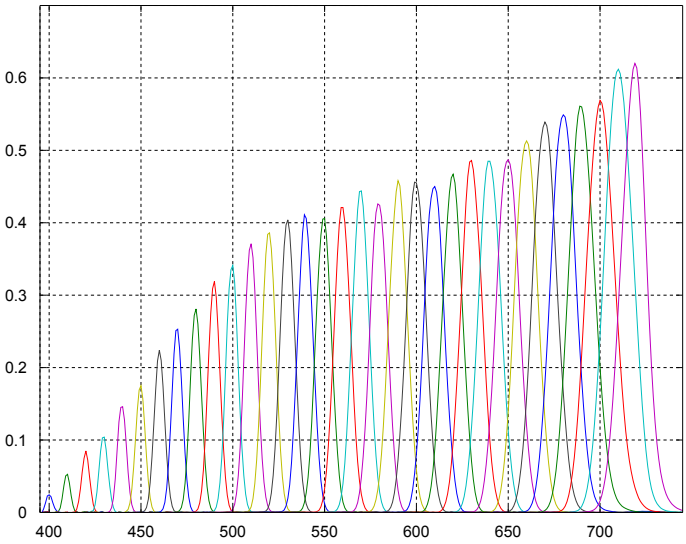

Figure 6.4: CRI VariSpec LCTF transmittance for a selection of 33 channels [56].

6.1.3 Integrated Sphere

The integrated sphere was located at the Institute for Natural Science and Mathematics (INM) of Prof. Dr. Bernd Jödicke at the HTWG Konstanz. The sphere was in a laboratory which could be darkened. As we were not the only research group using the laboratory, we were only allowed to use it on schedule. This restricted the time we could perform our experiments.

In order to use the sphere with our devices, several mountings had to be sketched and built. Figure 6.5 illustrates the setup used in our experiments in which the sphere was

involved. One can see the different devices connected on special mountings, like the "table" where the camera is connected to the sphere, or the high silver feet on which the monochromator stands. One could replace the PCO.Camera 4000 in the image by the AVT Bigeye G-132B or the spectrometer for a different experiment.

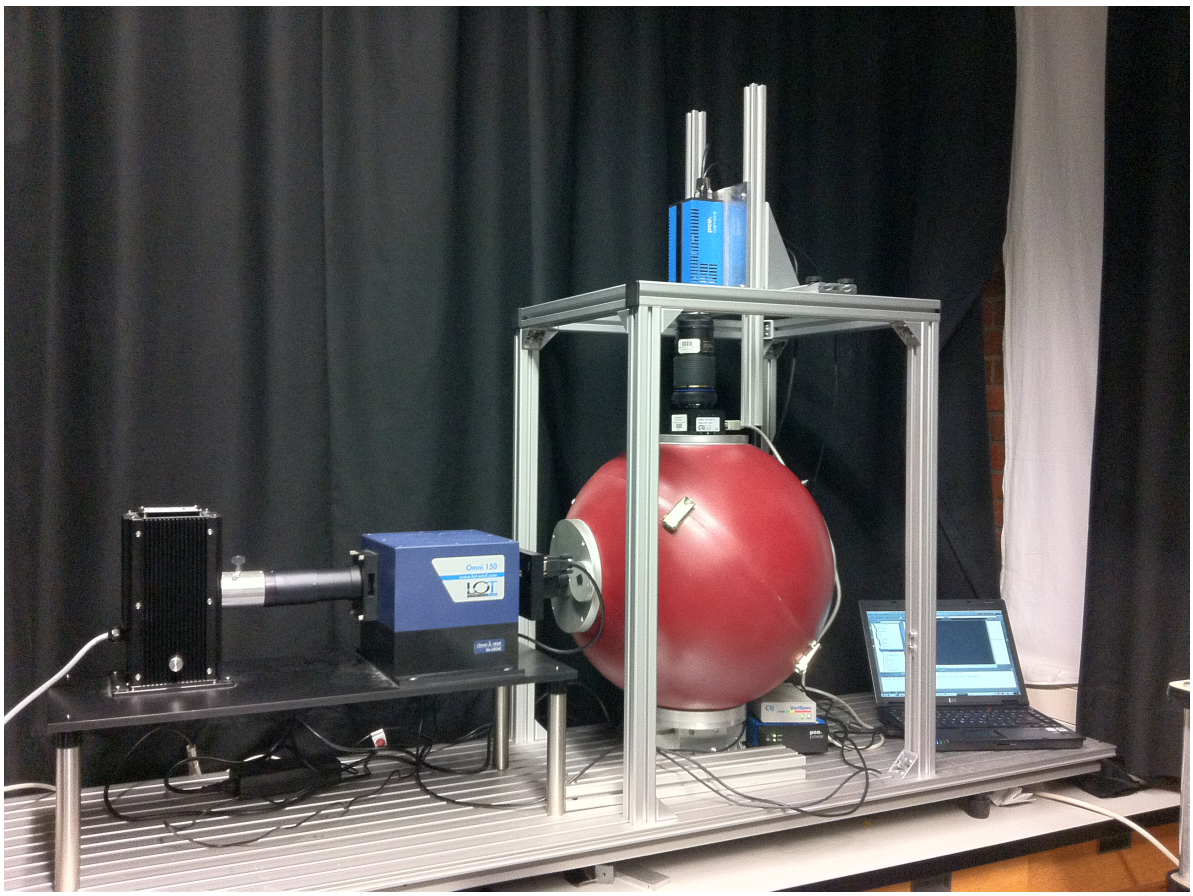

Figure 6.5: Experimental setup of monochromator, sphere, filter, and PCO.Camera 4000.

6.1.4 Monochromator

During the calibration process we used a monochromator to control the spectral radiance of the light source. The LOT Omni-l 50 is a direct drive scanning monochromator system that is connected with a grating turret LOT 10-150W where the halogen light source is located for passive cooling [57, 58]. Cooling improves the stability of the spectral output of the lamp drastically. Unlike fan-chilled housings, this housing uses natural convection cooling. This method is vibration free, which results in a more stable lamp

output.

For the light source there is a digital meter to ensure repeatable voltage settings. As light source an Orsam HLX 64623 Halogen Lamp was used, which has a power of 100W at 12V. The maximum aperture ratio of the Omni-l 50 is f/4.2. It is controlled through a USB 2.0 interface. Internally, the monochromator uses an asymmetric in-plane Czerny-Turner configuration, which was introduced in section 4.2. Figure 6.6 shows the monochromator (blue box) together with the cooling tower.

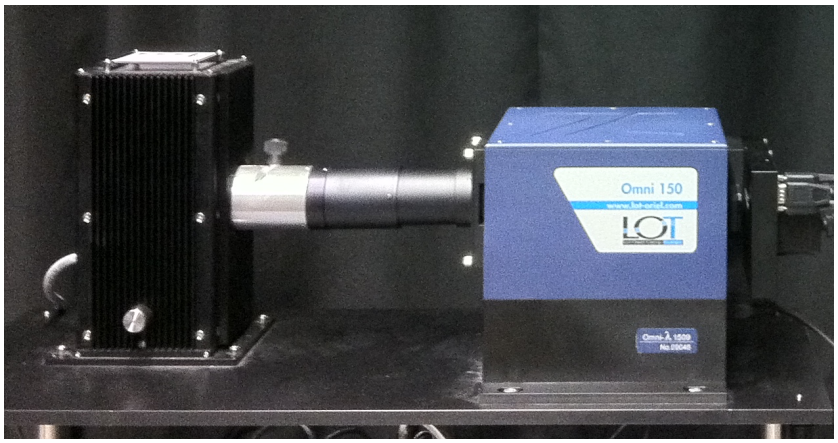

Figure 6.6: LOT Omni 150 connected to a LOT 10-150W halogen light source [57, 58].

6.1.5 Spectroradiometer

To calibrate the monochromator and the multispectral imaging system, respectively to validate our measurements, a spectroradiometer was required. For this purposes we used a Konica Minolta CS-2000 [59]. This polychromatortype spectroradiometer has the ability to measure 100000:1 contrasts and is designed to pick up low luminance ranges that reach 0.003cd/m2. The CS-2000 can measure a spectrum in the wavelength from 380 to 780nm with a precision of +/-0.3nm and a spectral bandwidth of 5nm or less. The spectrometer has the three free selectable measuring angles 1°, 0.2°, and 0.1°. Figure 6.7 provides an image of the device.

Figure 6.7: Konica Minolta CS-2000 spectroradiometer front and rear[59].

6.2 Software

Before we could use the devices in our experiments, they had to be integrated into a common framework. In the IOS framework of the Institute for Optical Systems at the HTWG Konstanz all the devices of the institute are included to be able to combine them whenever they are used together. The framework is implemented using the Qt framework and CMake. The documentation is written in Doxygen. The major part of this work was done during my master project.

The different device APIs were complicated to handle. Some of them have initially been designed for Windows. Only an incomplete and faulty implementation for Linux was available. This had to be adapted and debugged in order to work with our system. After the APIs worked correctly they were integrated in the framework. The first tests included initialization, initial readout of the camera settings, and at a later point basic image acquisition without advanced settings, e.g. automatic exposure control. After this step was achieved, the script was adapted and included in the iOS framework. After a few months of work, finally the following widgets were available in the framework:

- automatic initialization of all devices,
- taking single images or images in a sequence,
- preview of images acquired by the camera,
- saving images to 16 bit Tiff using Libtiff files for post-processing,

- and a sequencer tool for automatic acquisition of images under given exposure range, filter stepping, and monochromator stepping.

Figure 6.8 shows a screenshot of the main window together with the sequencer tool. In this tool all our experiments were either implemented to run on button click or could be freely configured by selecting different options. After the configuration, the experiments were running on their own. This allowed us to conduct even long experiments around 30h.

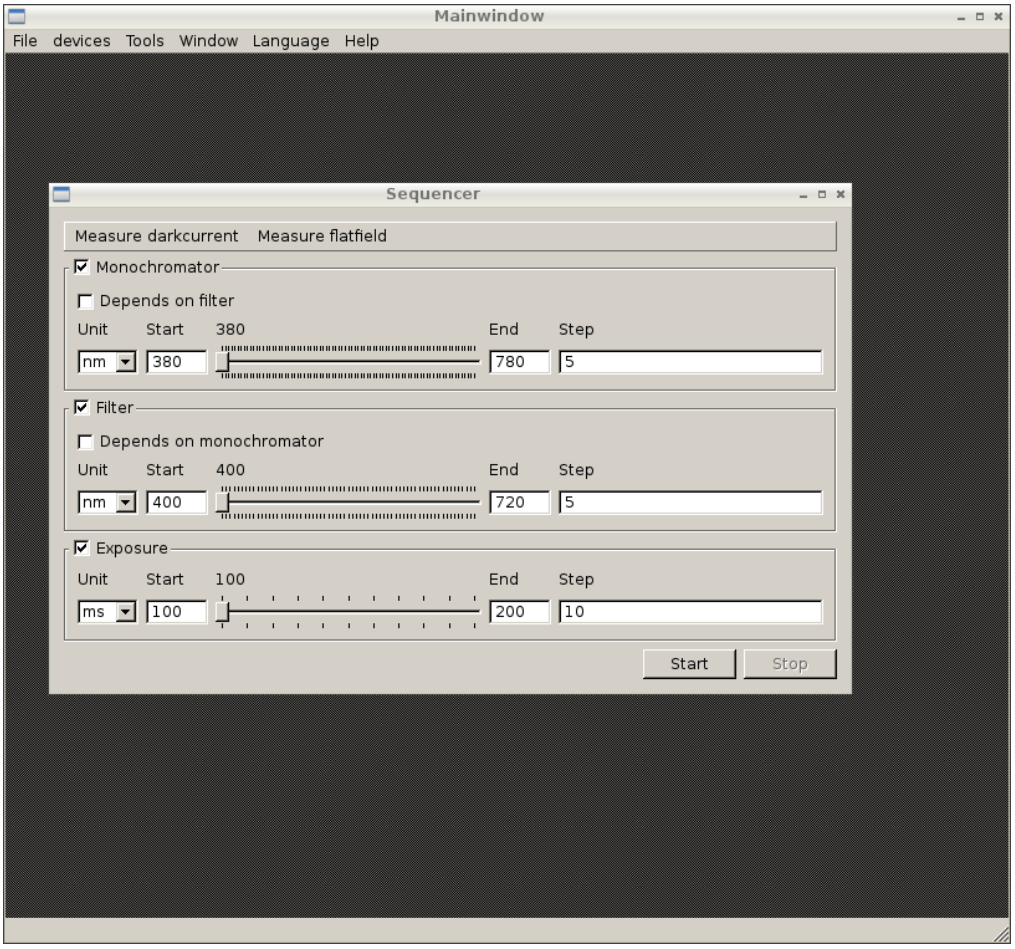

Figure 6.8: IOS Framework and the sequencer tool.

6.3 Conclusion

This chapter discussed the various devices used for our multispectral imaging system and the motivation why we chose these. In summary, our multispectral imaging system

consisted of an AVT Bigeye G132 as camera, a Computar M7528-MP as lens, and a CRI VariSpec LCTF as filter. For calibration we used a LOT Omni-l 50 as monochromator together with a LOT 10-150W to contain the light source, and an Orsam HLX 64623 Halogen Lamp to produce monochrome light. The light was made diffuse in an integrated sphere. Finally a Konica Minolta CS-2000 was used to calibrate the monochromator and the multispectral imaging system, and further to validate our measurements. The devices were integrated in the IOS framework. This software allows to run a selection of predefined experiments without requiring manual changes of the settings in between. The experiments conducted will be discussed in detail in the next chapter.

Chapter 7

Experimental Work and Results

Contents

The different devices presented in the last chapter were used for various experimental setups. First we had to examine the properties of these devices, such as the spectral radiance of the monochromator or the camera linearity. The information gathered here allowed us to properly calibrate our models. We then examined the camera for noise and collected the reference images for noise correction. Finally we could determine the multispectral imaging system spectral sensitivity. To check if our spectral reconstruction model was accurate, we validated it with a MacBeth color chart and the spectrometer.

7.1 LOT Omni-l 50 Settings and Offset

Before we could use the LOT Omni-l 50 for our experiments, we had to understand the effect of its settings. First of all we tried different configurations of front- and back-slit sizes in mm. Changing these values has an impact on how much of the separated light can pass at each side of the light ray. Through this the shape of the generated spectral curve changes as more or less of the original spectrum of the light source can get through. Furthermore, the intensity of the output is increased or decreased.

We adjusted the monochromator to output light at different wavelengths, which was recorded by the spectrometer. Results for combinations of different front- and back-slit sizes are shown in figure 7.1. Increasing the sizes of the front-slit had a large impact on intensity and an impact on the shape of the curve. This can be seen when comparing plots on the next page in figure 7.1a and 7.1b, respectively 7.1c and 7.1d. Changing the back-slit, on the other hand, had a minor impact on the shape, see figures 7.1b and 7.1c. We chose to use a front-slit size of 2mm and a back-slit size of 6mm for calibration, as this produced the highest intensities while having smooth Gaussian shaped curves. This can be observed in detail in figure 7.1d and overall, for monochromator output intensities between 400nm and 720nm with a 10nm stepping, in figure 7.2.

When analysing the monochromator data obtained through the spectrometer in more detail, we realised an offset of the peak of the measured spectral curve compared to the initial set value. We used these peaks to calibrate the output response of the monochromator to the actual set value by establishing an offset. Figure 7.3 gives an overview of the spectral curves for different wavelength settings. As an example, for a wavelength of 400nm the peak of the actual output is around 395nm (red curve).

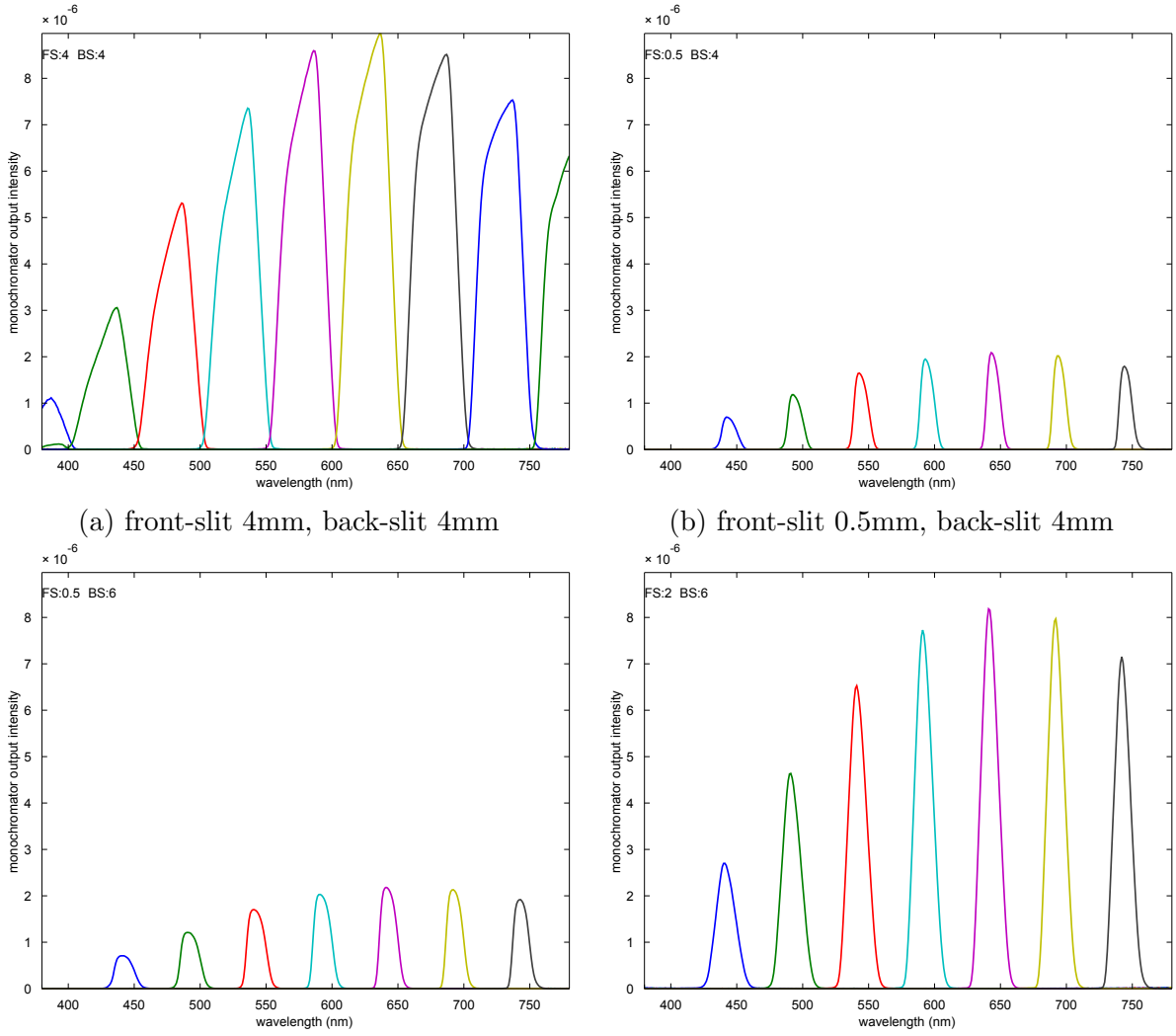

(a) front-slit 4mm, back-slit 4mm

(b) front-slit 0.5mm, back-slit 4mm

(c) front-slit 0.5mm, back-slit 6mm

(d) front-slit 2mm, back-slit 6mm

Figure 7.1: Output intensities of the LOT Omni-l 50 for different front- and back-slit settings measured with the CS-2000.

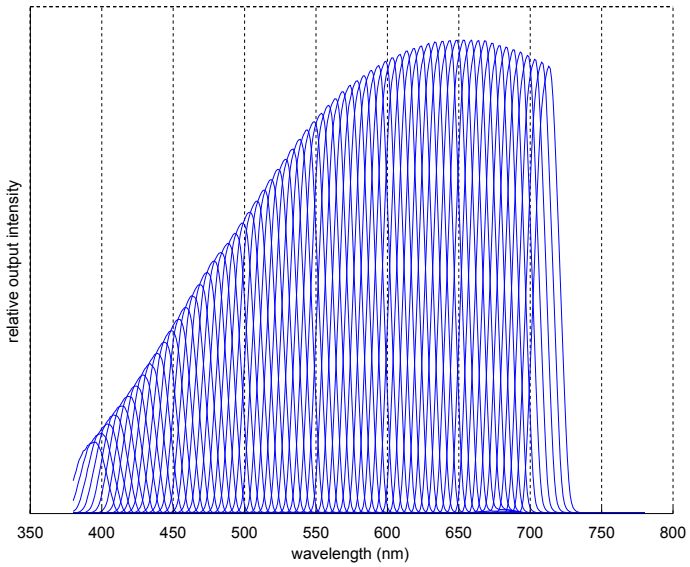

Figure 7.2: Monochromator LOT Omni-l 50 output intensities at a wavelength interval of 400nm to 720nm and a stepping of 10nm measured with the CS-2000.

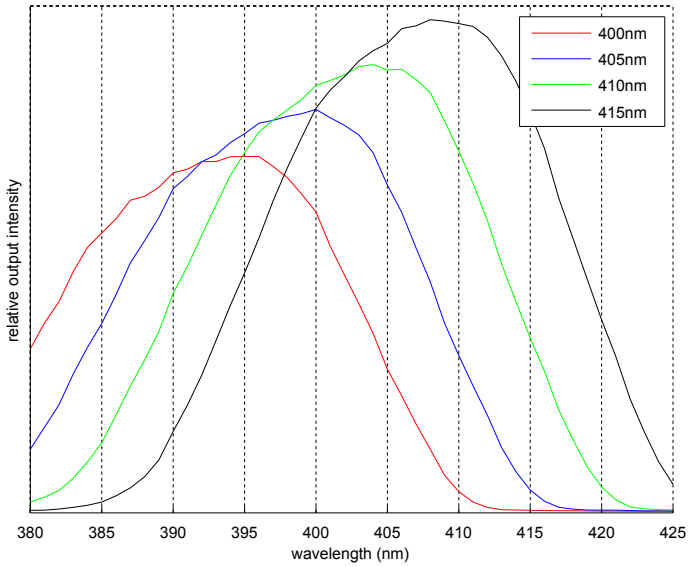

Figure 7.3: Monochromator LOT Omni-l 50 output intensities at different wavelength settings measured with the CS-2000.

7.2 AVT Bigeye G132 CCD Linearity

All of the models are based on the assumption that the CCD of the camera used in the multispectral imaging system is linear. This is rather important as otherwise the models had to be adapted for non-linearity. To check for linearity, three factors were examined: the halogen light source, the camera, and the filter with different wavelengths from 500nm to 700nm. We took exposure sequences with an output depth of 8bit. Figure 7.4 shows the results of this experiment. We only used patches from the center of the images, since no noise correction was done so far. The mean values of the patches are plotted for different exposures at given filter setting. One can see that the camera response is linear for all channels. Each sequence reaches the maximum at 255 (2^8 bit depth). This is where images are over-exposed.

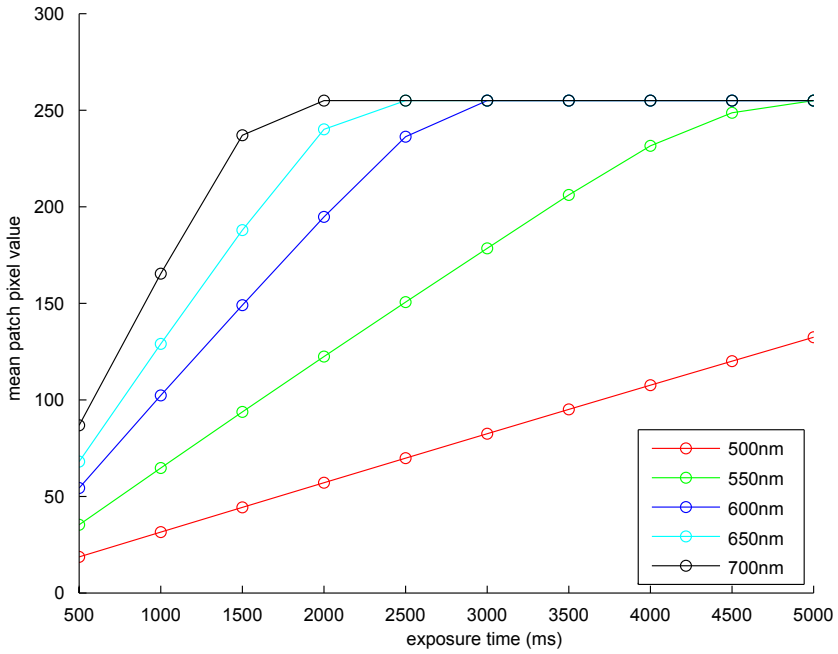

Figure 7.4: The mean patch AVT Bigeye G-132B camera response for different exposures.

7.3 AVT Bigeye G132 Flat Field Correction

Next we examined the noise of the AVT Bigeye G132 CCD. This correlates to the compensation methods given in chapter 5. For each of the different sources of noise, read out, dark frame, and vignetting, several experiments have been realised.

7.3.1 Read Out Noise

For the read out noise we conducted two experiments. First we examined the non-constant part of the read out noise. Therefore we took a sequence of 200 images of the integrated sphere with the Osram HLX 64623 halogen lamp as light source. The filter was set to 700nm, exposure of the camera to 450ms, focal length to f1.2, and aperture to f/2. In figure 7.5 we plotted the standard deviation (std) of the whole image for a mean image of a sequence of n images. One notices that the standard deviation drops quickly and does not change significantly anymore for more than 30 images. We concluded that to reduce the variable part of the read out noise we have to take 30 images of the same scene. More images do not reduce the noise significantly.

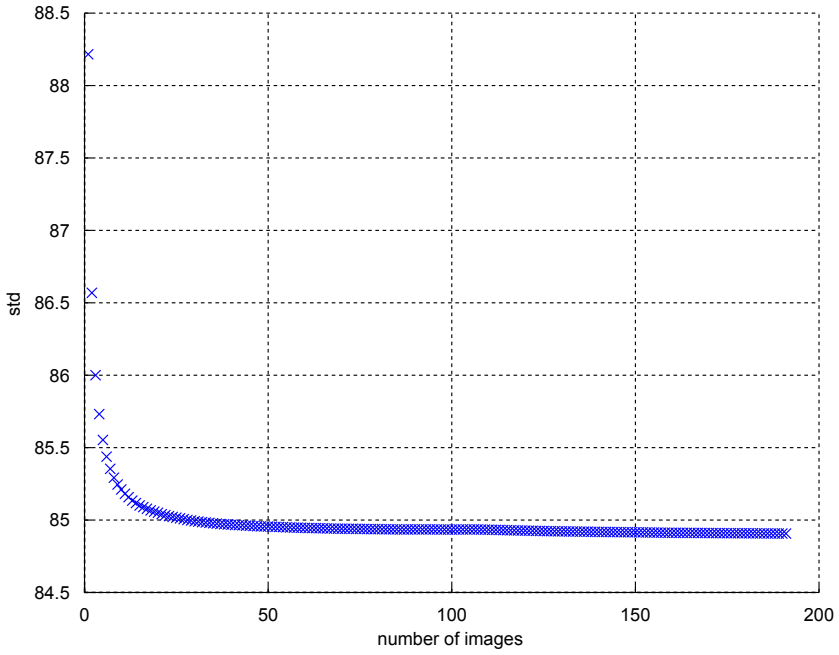

Figure 7.5: The std over mean of n images.

In practice this value is difficult to manage. The images required for the calibration process take circa 25 hours to record due to reasons that will be discussed in section 7.4. Increasing this time by a factor of 30 was not possible in practice, because of the accessibility to the dark room where our experiments were set up. For the recording of natural scenes, moving objects come into mind which represent trouble for a mean image and result in further inaccuracies due to ghosting effects.

Secondly we recorded the bias image, as described in section 5.1. We set the exposure of the camera to the minimal value of 81ms. The lens cap was put on and the recording took place in a dark room. We then took a series of 30 images. The mean image of this series is the bias image. The mean value over all pixels of the image is 102.5. The standard deviation being 1.3 is very small. Figure 7.6 displays the image with false colors of a heat map. The different colors indicate different pixel intensities. The actual value is given by the color bar. All further calculations include read out noise correction through this bias image.

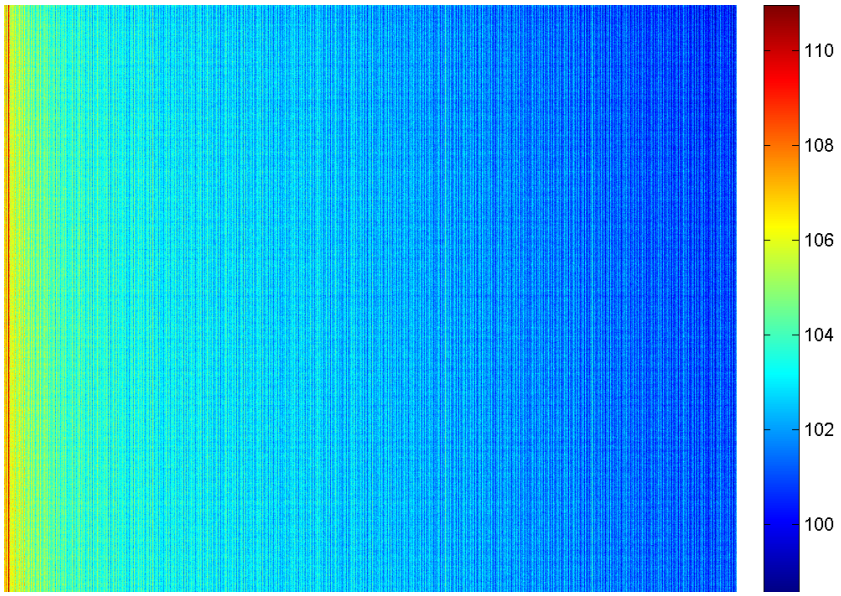

Figure 7.6: Bias image plotted with a heat map.

7.3.2 Dark Current

Next we examined the dark current (compare section 5.2). For this purpose we recorded a series of 30 images for different exposures. The lens cap was on the optics, the room was without light. The images were corrected for bias. Afterwards we took the mean

of the series. In figure 7.7 the mean of the resulting dark current images (dark frames) is plotted. The mean values stay relatively constant over the different exposures, only varying between 0.1 and 0.7 pixel intensities. Since this value is very small we decided not to correct for dark current.

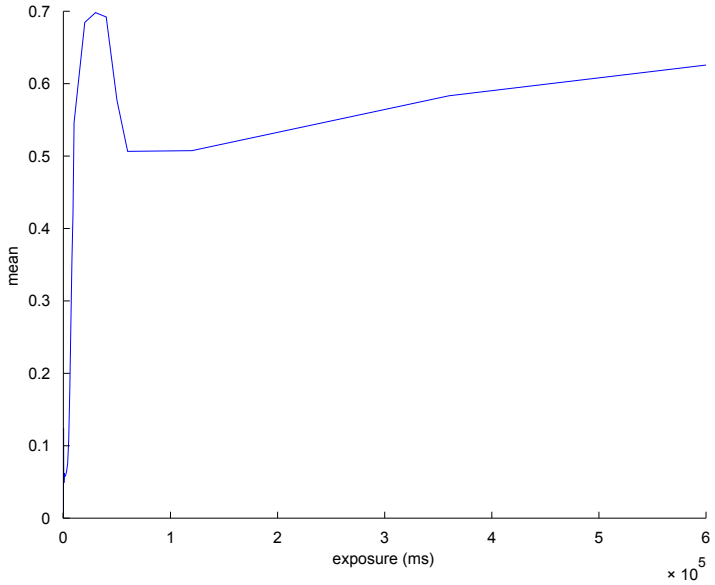

Figure 7.7: The mean values of dark frame images for different exposures.

Thereafter we were interested in the question how the uncertainties in the measurements change for longer exposures. In the left of figure 7.8 we plotted the standard deviations for the same dark frames as before. The x-axis in the plot is logarithmic in order to be able to compare small and large exposure times. One can see that the standard deviation stays constant until 30,000ms (30s). It then starts to grow. In the right image we have a regular x-axis scaling were we can observe a rather linear growth in standard deviation. From this we conclude that the measurement uncertainties grow with exposure time duration.

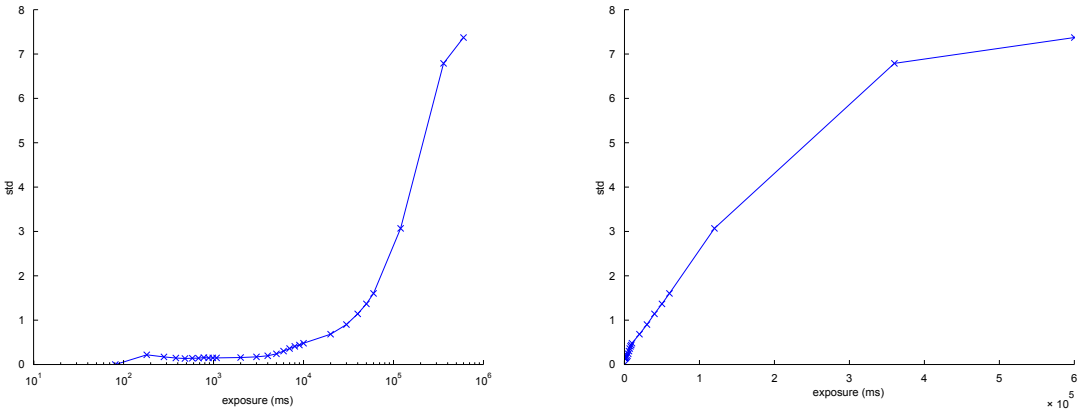

Figure 7.8: The std of dark frame images for different exposures (x-axis scaled logarithmic in the left image).

7.3.3 Vignetting

We conducted several experiments to examine the effect of different settings or physical positions on vignetting (see section 5.3). We started with analyzing the effect of vignetting at different positions. For this, we used the halogen light source together with the integrated sphere for a homogeneous, diffuse light. We opened the top of the sphere in order to reduce the effect of the sphere onto vignetting. We moved the multispectral imaging system to three different positions and took 200 images at each position. The exposure was set to 450ms, the filter to 700nm, focal length to f1.2, and aperture to f/2.8. All images were noise-corrected besides vignetting.

Table 7.1 contains the means and the standard deviations of three different positions which are almost the same. We found that the resulting images were very stable. The mean and standard deviation just change by a very small amount. Figure 7.9 displays the three images generated together with a heat map indicating the values of the different pixel responses.

Pos	1	2	3
mean	2720	2728	2734
std	84	84	83

Table 7.1: Means and standard deviations of images taken at different positions for vignetting.

Vignetting depends on focal length, aperture, and physical position of the optics (com-

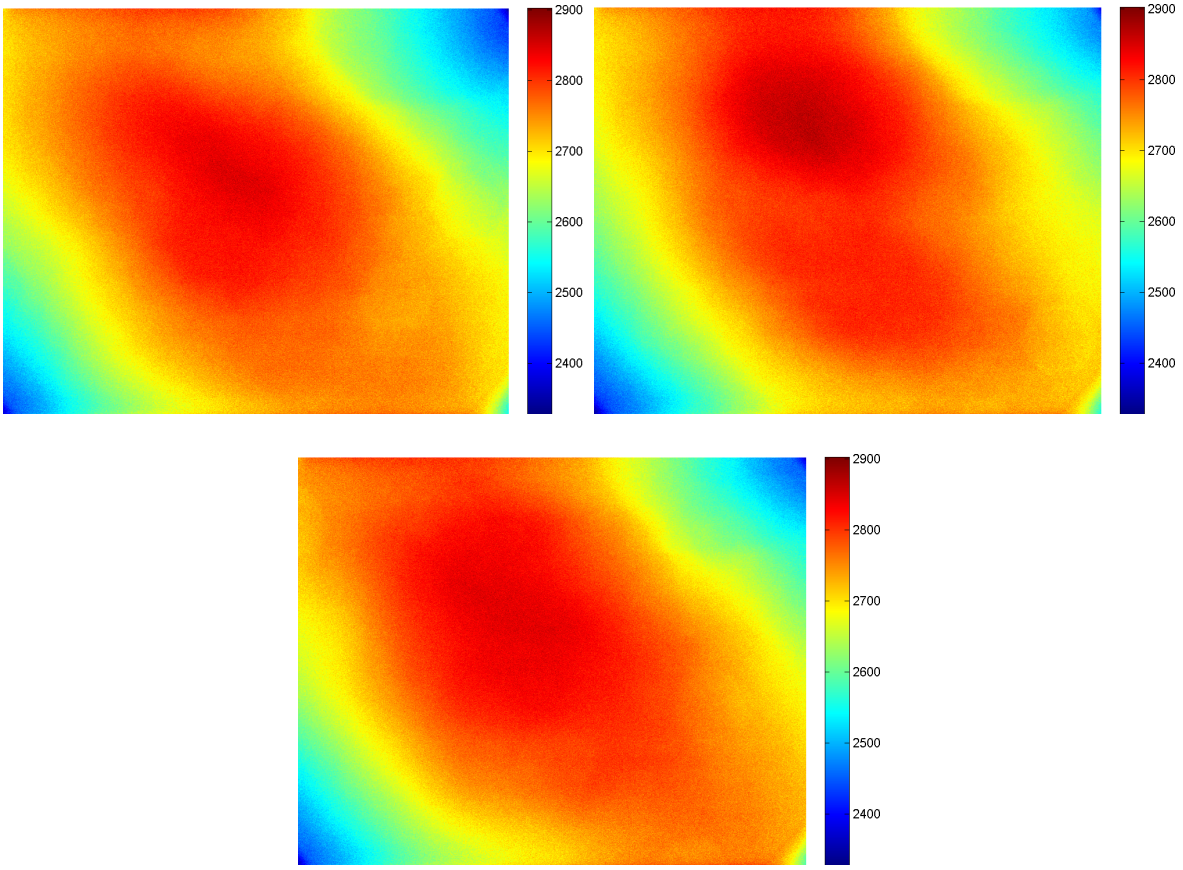

Figure 7.9: Output intensities of the LOT Omni-l 50 for different front- and back-slit settings measured with the CS-2000.

pare section 5.3). In a series of experiments we used homogeneous light to examine these effects. Monochrome light at 680nm was used. The filter was adjusted to 680nm and rotated physically during the experiment. The images were corrected for noise besides the effect of vignetting. Since the images were recorded with different sizes for aperture, we had to alter the exposure to avoid under- or over-exposure. Therefore the images were divided by the exposure to be evenly scaled. Table 7.2 provides an overview of the different settings used in the experiments, as well as the means and standard deviations for the resulting images.

First we wanted to see the physical effects of the filter. To achieve this, we rotated the filter by 90ř for the same focal lengths and apertures. Figure 7.10 displays the resulting images with a heat map of the images generated from experiment 1 and 4. The figure distinctly illustrates that the blue area in the top right and the green area in the top left rotate with the filter. The shape of the inner red area rotates as well. There is a

experiment	1	2	3	4	5
rotation (degrees)	90°	0°	0°	0°	0°
focal length (mm)	1.2	1.2	2	1.2	2
aperture (f/x)	4	2.8	2.8	4	4
exposure (ms)	25000	12000	12000	25000	25000
mean	0.1305	0.2309	0.2295	0.1333	0.1428
std	0.0045	0.0135	0.0229	0.0038	0.0058

Table 7.2: Means and standard deviations of images taken at different positions.

small effect of the integrated sphere present in these images.

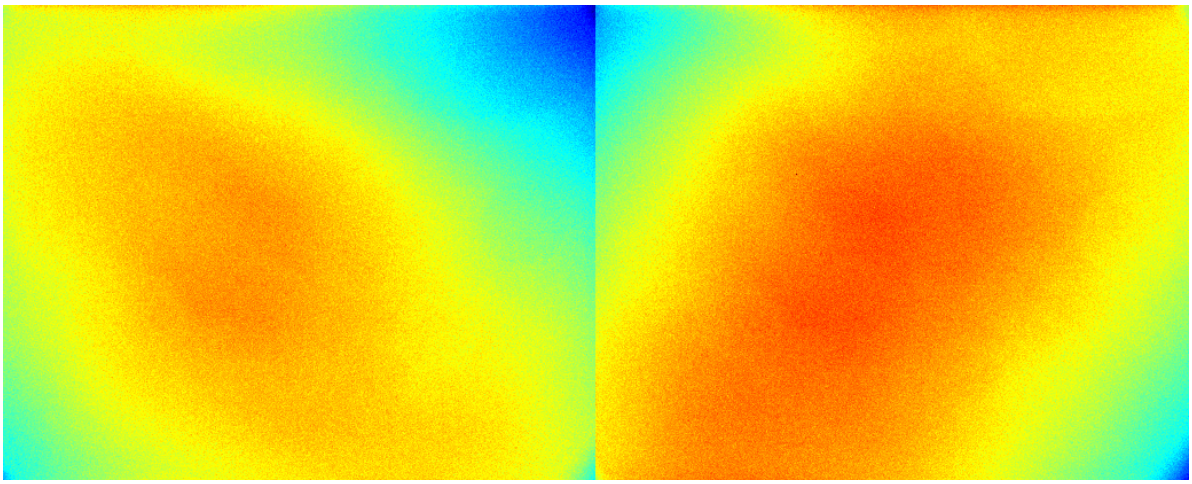

Figure 7.10: The effect of physically rotating the filter by 90ř for f1.2 and f/4.

Afterwards we investigated the effect of focal length on vignetting. We compared the images from experiment 2 and 3 by a heat map. In these experiments the aperture stayed the same and the focal length was increased from 1.2mm to 2mm. The results are depicted in figure 7.11. The vignetting effect increases with the inhomogeneous areas in the corners, growing for a higher focal length. The standard deviation increases from 0.0135 to 0.0229. This supplies evidence that a higher focal length increases the effect of vignetting.

Finally we determined the effect of aperture. For this we compared the images from experiment 3 and 5. This time we did not change the focal length, but increased the aperture from f/2.8 to f/4. Figure 7.12 displays the results of this experiment. The standard deviation drops drastically from 0.0229 to 0.0058. One can see that an increased aperture reduces the effect of vignetting.

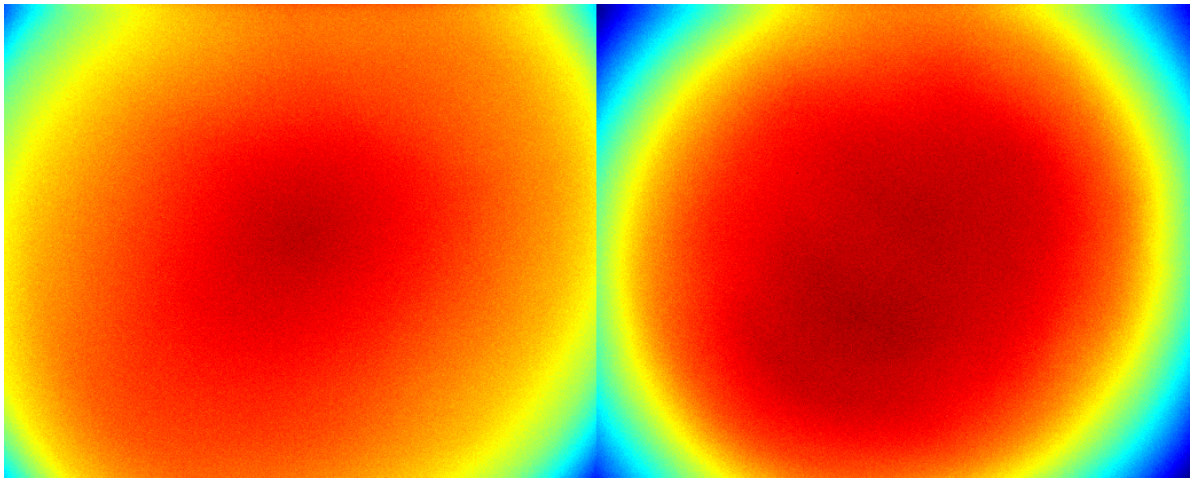

Figure 7.11: The effect of focal length for aperture f/2.8 in both, focal length f1.2 in the left and f2 in the right image.

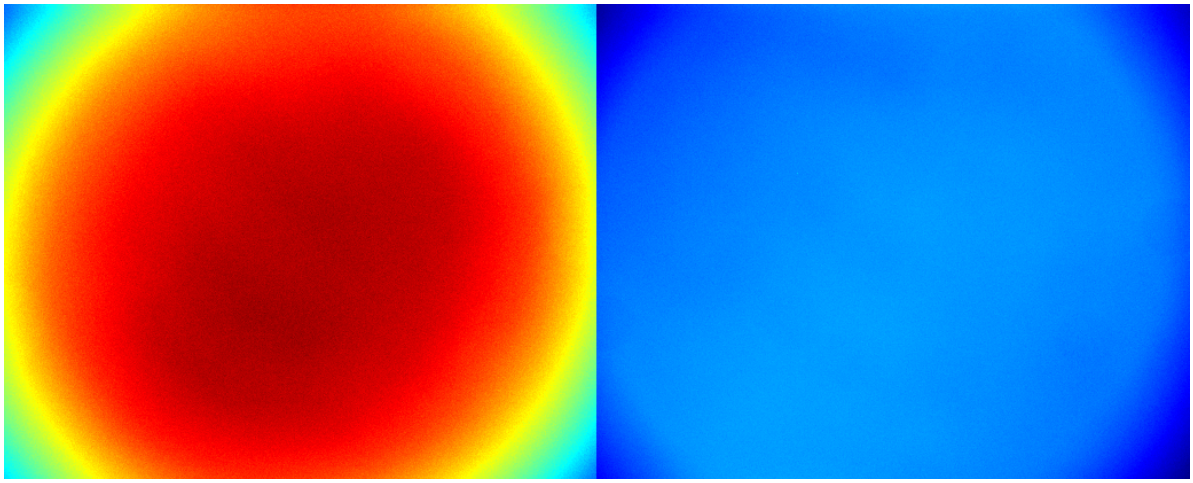

Figure 7.12: The effect of aperture for focal length f2 in both, aperture f/2.8 in the left and f/4 in the right image.

As corollary of this experiment we recorded a reference vignetting image for every focal length/aperture pair we used during calibration and validation. We then used these images for our noise-correction algorithm. The fact that vignetting is reduced drastically for larger apertures reduces the overall noise for higher light intensities. This means for us that the effect is more significant under laboratory conditions than during the recording of natural scenes, since more light is present in nature and, hence, the aperture value is increased (the actual aperture is made smaller).

7.3.4 Quality Measurement

To measure the performance of our noise correction, we performed it on several images. Figure 7.13 illustrates an example of an image corrected for noise. The image on the left was taken for monochrome light at 660nm, filter adjusted to 660nm, and an exposure set to 5000ms. It was then corrected for noise. The result of the noise correction is shown in the right image. Overall the mean dropped from 1150 to 1139 and, crucially, the standard deviation from 65.3 to 19.4. Overall the noise correction improves the quality of the images drastically.

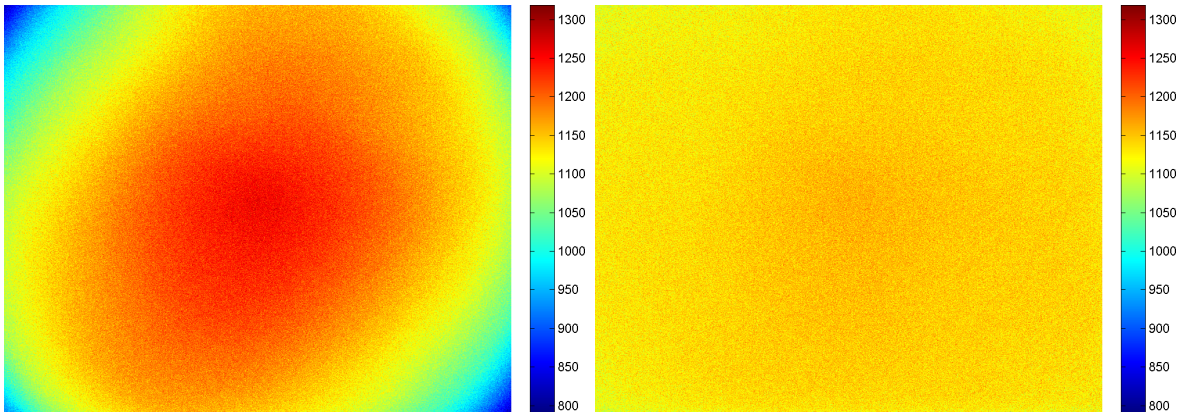

Figure 7.13: Image before and after noise correction.

7.4 Spectral Calibration

After the initial experiments we now were able to begin with the spectral calibration. This provides information about the spectral sensitivity of the multispectral imaging system to different wavelengths. With this information the spectra of a scene can be calculated from the system response.

The experimental setup for the channel responses should be the following: The system is set to record a specific channel. The monochromator is used together with the integrated sphere to produce homogeneous monochrome light. Next the monochromator is stepped over the whole spectrum of interest, in our case from a wavelength of 400nm to 720nm. The smaller the steps, the more precise the measurements. At every step several images should be taken to compensate for read out uncertainties.

In practice, however, we could not follow this approach in detail. For small wavelengths the light intensities produced by the monochromator are very low (see figure 7.2). Simultaneously, the filter transmittance at this point is very small (see section 6.1.2 figure 6.4). This means that the intensity of the light reaching the CCD at these wavelengths is already rather low. Furthermore, the sensor sensitivity for these wavelength is small as well (see section 6.1.1 figure 6.2). This means that the recording time for an image at these wavelengths has to be extremely long. In practice they reached around 20min, decreasing with increasing intensities, respectively for higher wavelengths. This would result in measuring several weeks.

Since we could not measure for so long, we chose to record in an interval from -33nm to +33nm of the specified wavelength with a stepping of 3nm. With these settings the recoding time was reduced to 30h. However we could not compensate for the measurement uncertainties of the read out noise by recording several images. The lens was set to a focal length of f1.2 and an aperture of f/2.8 which made the light diffuse. The light was recorded in a following experiment with the spectrometer.

After the images were recorded, they were corrected for bias and vignetting. Furthermore every image was divided by the exposure time it was recorded under to bring the data to an even scale. This was possible due to the linearity of the sensor.

The spectral reconstruction models presented in chapter 3 were designed for specific illuminants to estimate the spectral reflectance. To remove the effect of the illuminant on the data we normalised the multispectral imaging system response against the actual light intensity recorded with the spectrometer. Hence, our system cannot estimate the spectral reflectance of objects but their spectral radiance. This allows us to record any scene independent from the illuminant. If the illuminant is known we then in turn can estimate the actual spectral reflectance of objects again.

In order to cope for the missing measure in the range from -33nm to +33nm of the channel we used smoothing splines to interpolate the actual sensor response. Values outside of this interval were set to 0 for every channel. Figure 7.14 is the resulting plot for the estimated multispectral imaging system spectral sensitivity. The blue dots indicate our measurements. The red line is the interpolated curve that gives the spectral sensitivity. Furthermore this data allows us to build the spectral sensitivity matrix $\mathbf{\Theta}$ (compare section 3.2.2). For interpolation based methods the calculated channel sensitivities allow us to normalize recorded data by dividing through the peak measurements, as well as providing knowledge at which wavelength the measured data points are located (compare

section 3.2.4).

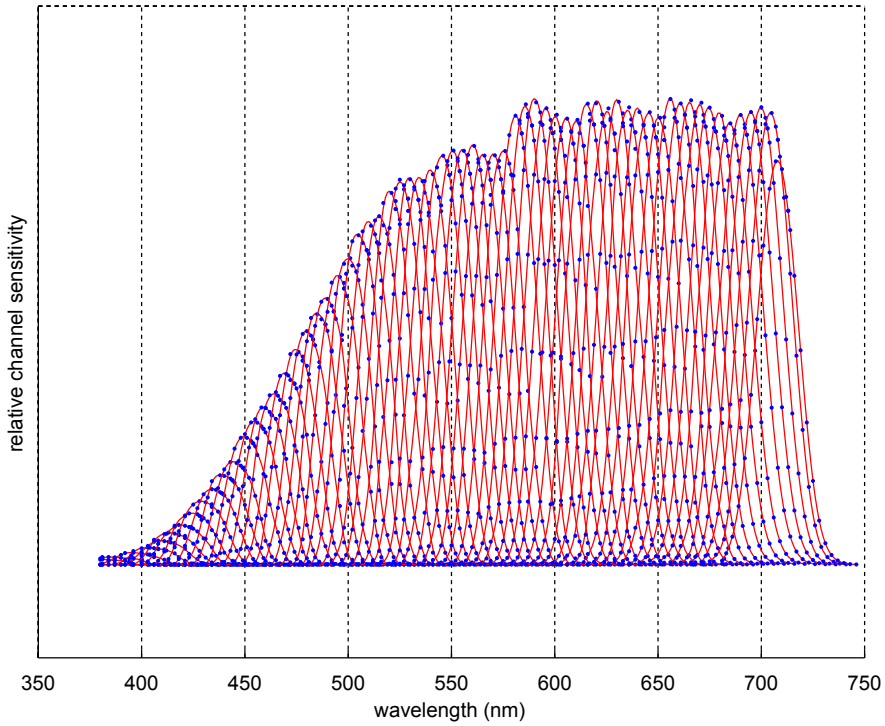

Figure 7.14: Spectral sensitivity of the multispectral imaging system.

7.5 Validation

For the validation of the estimated spectral sensitivity we used nine patches of the MacBeth color chart. The halogen lamp used as the illuminant was warmed up prior to recording, thereby ensuring stability. First the patches were recorded with the spectrometer in a dark room. On another day we recorded the same patches with the multispectral imaging system for different channels. Exposure times were set in a manner that the images were not over-exposed. Figure 7.15 on the next page shows several of the images recorded at different filter and exposure settings.

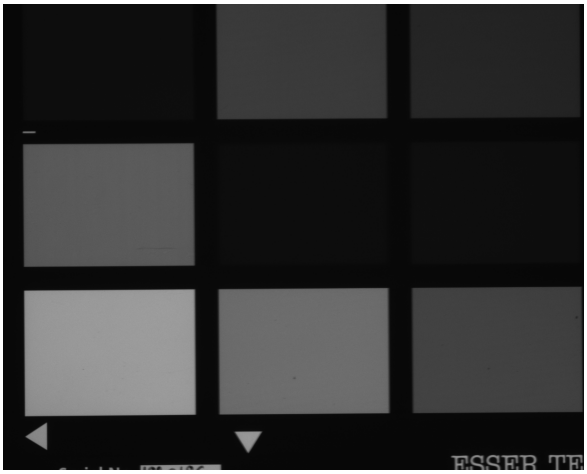

(a) filter 450nm, exposure 2081ms

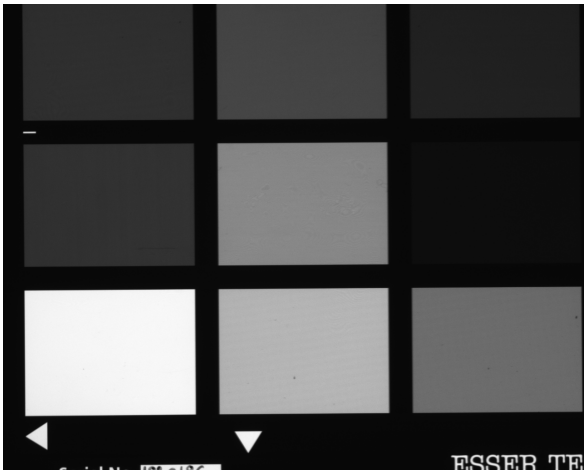

(b) filter 500nm, exposure 581ms

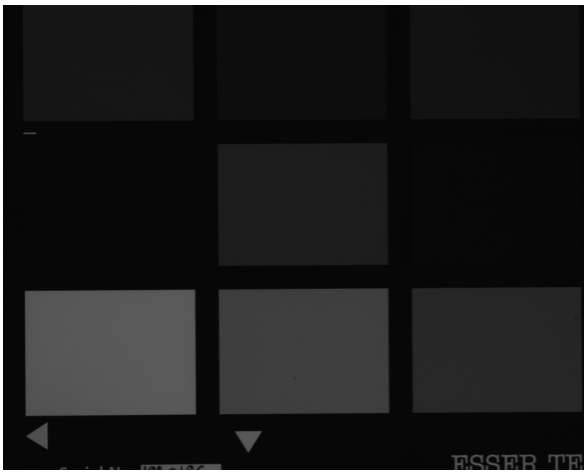

(c) filter 550nm, exposure 81ms

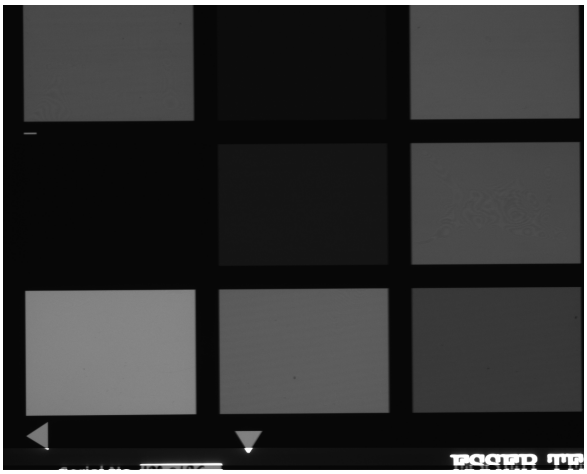

(d) filter 600nm, exposure 81ms

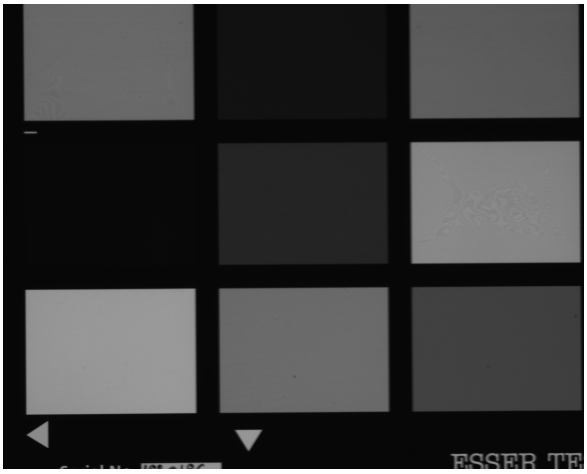

(e) filter 650nm, exposure 81ms

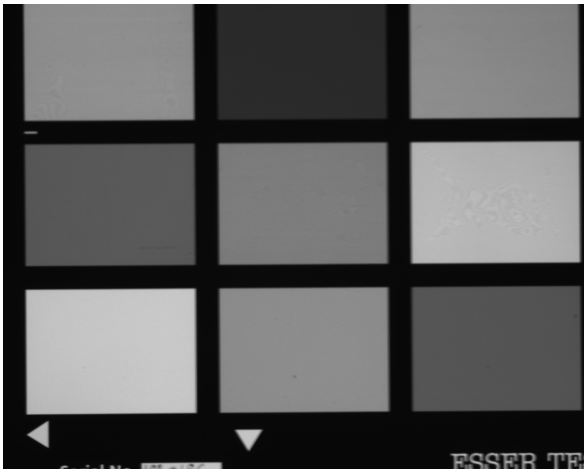

(f) filter 700nm, exposure 81ms

Figure 7.15: Images of the MacBeth color chart for different channels and exposures.

For each channel we recorded two images in order to reduce the read out noise uncertainties. The images were further corrected for bias and vignetting and divided by exposure. We took the mean of the camera response for the patches, normalized it, and used smoothing splines for spectral reconstruction. Figure 7.16 shows the results for the estimation of the spectral radiance of the nine patches. The blue line indicates the spectrum measured with the spectrometer. The red line indicates the spectrum as estimated with the multispectral imaging system.

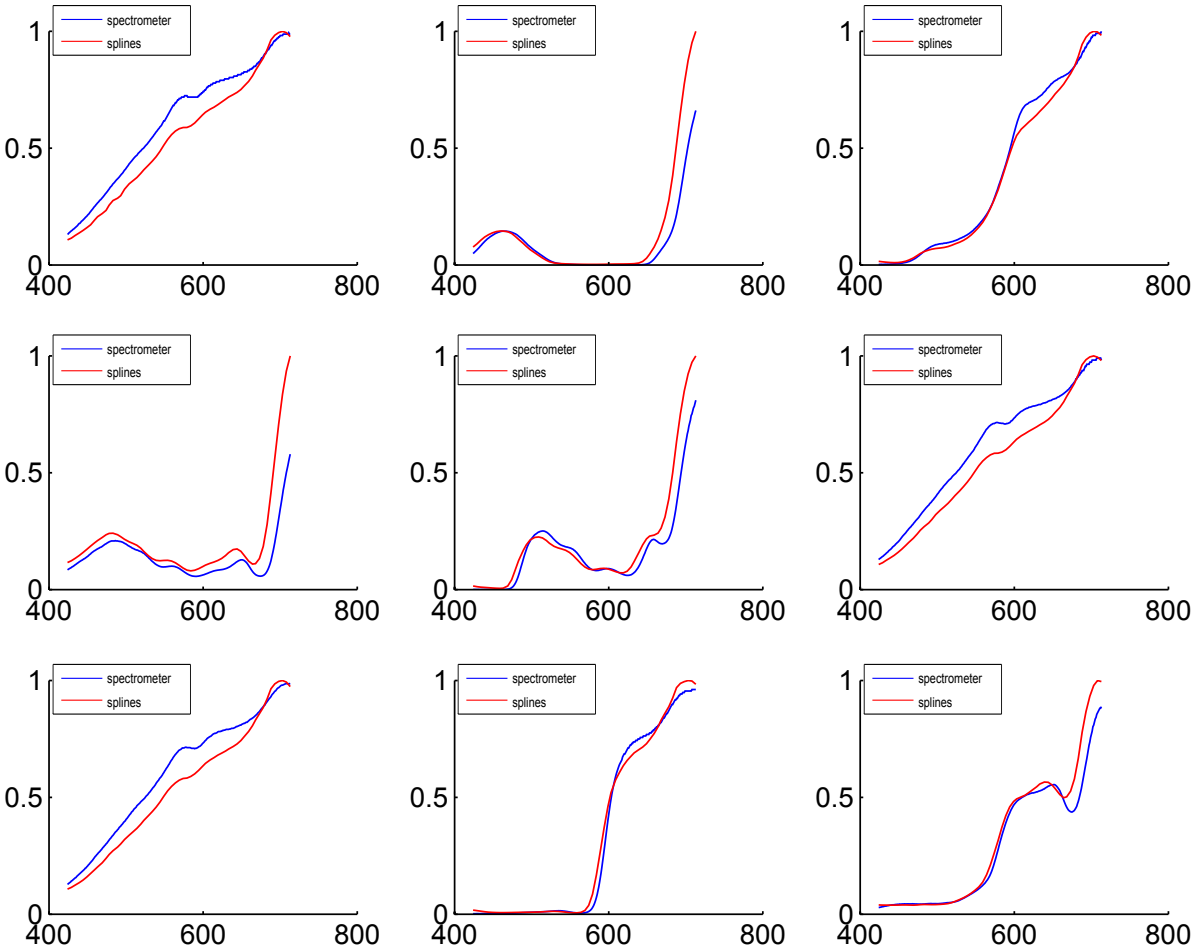

Figure 7.16: Spectral radiance measured by spectrometer and estimated with multispectral imaging system by smoothing splines.

Further we compared the the root mean square error (rms) for the nine recorded sample patches in table 7.3. We found that our rms of 0.0795 over all color patches is adequate compared to the theoretical performance of the CRISATEL project where an rms of

0.023 was achieved [7]. The general performance of the system is considerably accurate with some aberrations in the intensity. These could be either due to inaccuracies during calibration or to impureness of the color patches, which remains to be evaluated as a future task.

rms	0.080	0.118	0.034	0.133	0.091	0.079	0.079	0.034	0.068

Table 7.3: Root mean square errors of original and estimated spectral reconstruction through smoothing splines for the nine sample images.

Beside smoothing splines, we also used other spectral reconstruction methods for comparison. Initially we evaluated the quality of matrix $\mathbf{\Theta}$. Therefore we tried to estimate the spectral radiance theoretically through the spectral sensitivity matrix. The spectral curve recorded by the spectrometer was transformed into a camera response by multiplying it with $\mathbf{\Theta}$. We then multiplied this theoretical camera response by the pseudo inverse $\mathbf{\Theta}^+$. In figure 7.17 we plotted the original spectral radiance curve s as measured with the spectrometer (blue) and $\mathbf{\Theta}^+ \times (\mathbf{\Theta} \times s)$ (red). The resulting reconstruction of the spectral radiance proved to be very accurate as expected. This validates our matrix $\mathbf{\Theta}$.

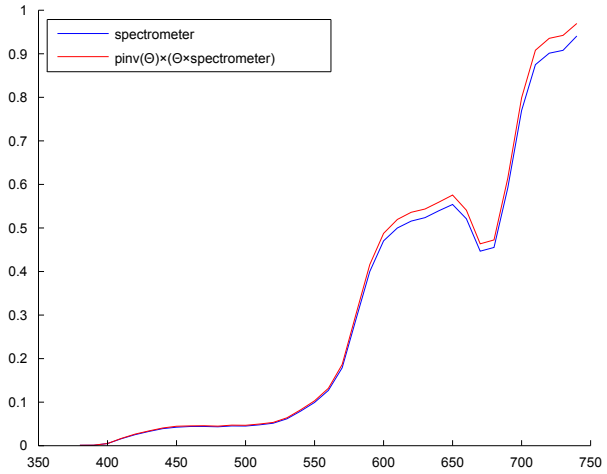

Figure 7.17: Spectral radiance measured by spectrometer and estimated with multispectral imaging system by taking $\mathbf{\Theta}^+(\mathbf{\Theta} \times s)$.

We then evaluated the pseudo inverse $\mathbf{\Theta}^+$ times the camera response. As mentioned in section 3.2.2 the real spectrum $\mathbf{r}$ and its estimation $\mathbf{r}'$ are not guaranteed to be close by this method. This one can see in figure 7.18 where the estimation of the spectral radiance fails poorly.

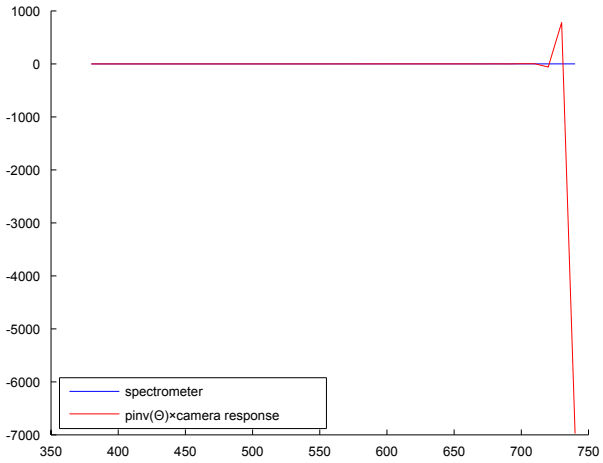

Figure 7.18: Spectral radiance measured by spectrometer and estimated with multispectral imaging system by pseudo inverse.

The measured data enabled us to use an indirect approach as well. We estimated the spectral radiance via the NNLS algorithm (see section 3.2.3.3) from the camera response and the channel sensitivity. The result for these calculations can be seen in figure 7.19. Although the estimated spectral curve follows the real spectral curve, it is not smooth. For this approach it might be necessary to have more than the 65 measurement pairs we had. As mentioned in section 3.2.3.1 around 200 should be used.

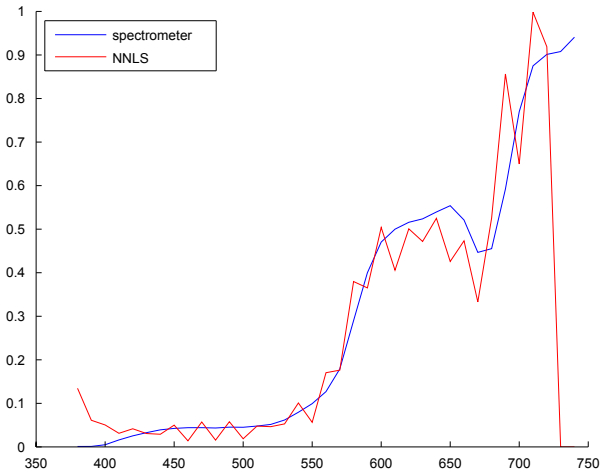

Figure 7.19: Spectral radiance measured by spectrometer and estimated with multispectral imaging system by NNLS.

7.6 Conclusion

The experiments presented in this chapter constitute the practical part of designing and implementing a multispectral imaging system. In a first step we examined the monochromator in order to receive precisely calibrated monochrome light that follows a Gaussian like curve. We then characterized the sensor with respect to linearity and noise. This was important in order to reduce errors during calibration and later measurements. During the next experiment we estimated the spectral sensitivity matrix $\mathbf{\Theta}$. Receiving the measurements required for the estimation was rather time consuming. Therefore we applied some optimizations to reduce the overall recording time. Eventually we could validate the estimated spectral sensitivity during a last experiment. The next chapter will conclude this thesis.

Chapter 8

Conclusion

This last chapter summarizes the thesis and provides my own thoughts on the topic and the results achieved. Furthermore, it presents some ideas about future work that could be pursued in context of the implemented multispectral imaging system.

8.1 Summary

Tricolor imaging does not suffice when in the need of analyzing and representing true colors. This is mainly due to metamerism, a phenomenon which causes two surfaces to appear the same under one illuminant but different under another. The metameric image reproduction workflow introduces many errors to the precision of color. These are caused by the different standards used for generating the tristimulus value and storing it, e.g. cielab or cie 1931 standard observer. This means that in tricolor imaging, color is always a matter of context. Therefore, color cannot be reproduced precisely under these circumstances.

Multispectral imaging aims at solving this issue. Instead of generating a tristimulus value, a multispectral imaging system samples a spectral curve of the recorded scene. This can either be the spectral radiance of the surface—the spectral radiance of the light source times the spectral reflectance of the surface—or, if the spectral properties of the light are known, the estimation of the actual spectral reflectance. These kinds of systems require three devices to work properly: a monochrome camera, an adequate lens, and a filter to individually select the channels.

In the camera model, the properties of all used devices are collected in the spectral sensitivity matrix $\mathbf{\Theta}$. For the camera response this results in the following equation which includes the camera model and matrix notation:

$$\mathbf{a} = \mathbf{\Theta r}. \tag{8.1}$$

The (pseudo) inverse $\mathbf{Q}$ can then be used to calculate the spectral reflectance $\mathbf{r}'$, respectively the spectral radiance.:

$$\mathbf{r}' = \mathbf{Q}\mathbf{a}. \tag{8.2}$$

There are several methods to estimate the matrix $\mathbf{Q}$. The direct methods are based on the previously known matrix $\mathbf{\Theta}$. Since the mathematical pseudo inverse does not guarantee $\mathbf{r}$ and its estimation $\mathbf{r}'$ to be close, more sophisticated methods are required which include regularization. Namely, these are the smoothing inverse, Wiener's filter, and Hardeberg's modified pseudo inverse.

The indirect, or learning based, methods use a different approach. They learn the pseudo inverse indirectly from a set of camera responses and corresponding actual spectral reflectances. These are recorded from color patches through the multispectral imaging system and a spectrometer. Methods based on learning include PCA respectively SVD, and the NNLS algorithm.

A third set of methods uses interpolation to calculate the spectral estimation directly from the camera response. However, in order to use interpolation, the camera response first has to be normalized to ensure the responses are scaled properly, compared to the spectral sensitivity of the system. Furthermore, information has to be present about the location the measurement points on the wavelength-axis of the different channels. There are many rather complex interpolation methods. Two of them were mentioned shortly in this thesis, namely spline interpolation and modified discrete sine transformation.

After discussing the mathematical models, chapter 4 introduced the devices used for multispectral imaging. The focus here did not lie on specific models, but on the overall technologies used. This background knowledge is important in order to be able to calibrate the system precisely. In the multispectral imaging system a monochrome CCD camera is used. CCDs are the state of the art in digital imaging. It is crucial to use a sophisticated, cooled camera, since regular consumer cameras are full of flaws and are not suitable for scientific purposes. Furthermore a lens is required, which should be selected dependent on the scenes that will be recorded. Finally, different methods for channel filtering were presented. Two approaches can be distinguished there, a set of filters mounted on a filter wheel versus a tunable liquid crystal filter. We found that the latter is more appealing due to its narrow, Gaussian shaped spectral transmittance curves. These are perfectly suited for multispectral imaging systems.

Beside the system devices, there were secondary devices required for calibration and

validation. These included the monochromator, color charts, and the spectrometer. They are used to either calculate the spectral sensitivity matrix $\mathbf{\Theta}$ for the direct methods, the pairs of camera responses and spectra for the indirect methods, or the information about the normalization and position of the camera responses for interpolation.

After I looked into the devices used in multispectral imaging systems it was realized that we required noise correction to compensate for error produced by the CCD or by the optical devices, i.e. the filter and the lens. This was the motivation to present the various sources of noise and the compensation algorithms to cope for them. These included read out noise, dark current noise, and vignetting. The rather simple flat field noise correction algorithm was presented as a combined result of the different approaches.

The theoretic part led over to my own experimental work. The multispectral imaging system presented consisted of three devices: an AVT Bigeye G132 as camera, a Computar M7528-MP as lens and a CRI VariSpec LCTF as filter. In several experiments the linearity of the camera was proofed and the devices were examined for noise. These helped generate the reference images for noise correction, bias image and different vignetting images. It was decided not to compensate for dark current noise, because its impact was marginal.

Along with these noise corrections the spectral sensitivity of the system was examined. This resulted in the generation of the matrix $\mathbf{\Theta}$ characterizing the system. Further the normalization matrix and the position of the camera response for different channels at the wavelength-axis were retrieved. We were able to validate the correctness of our results through a MacBeth color chart. This was the final experiment for the design and implementation of a multispectral imaging system.

8.2 Own Statement and Future Work

In this thesis I elaborated on the motivation and theory behind multispectral systems, and presented the practical work put into creating our own system. Both parts required much effort. Gathering information on the field of multispectral imaging is challenging. This is due to two factors. For one thing, the subject matter is rather complex and includes a great number of different models and methods used. For another thing, a lot of publications, and with them opinions, on the topic exist. The state of the art is

not apparent on first sight. I had to simultaneously understand multispectral imaging, integrate the devices, and design experiments. I encountered many difficulties, on the one hand due to the properties of the devices and on the other hand due to my lack of experience. However, in the end our group was able to design the right experiments for calibrating and characterizing our multispectral imaging system.

Now that the system is working properly, there are several more open tasks which raise interest for future projects:

- **Repetition of the spectral calibration:** We have done the calibration under several assumptions. Although the validation showed that the result is correct, an even more precise calibration is desirable. This would include a more narrow stepping of the monochromator in a wider wavelength interval, especially for the channels from 400nm to 420nm, as well as recording several images to compensate for the uncertainties in read out noise.

- **Inclusion of High Dynamic Range (HDR) Imaging:** Currently we are setting exposure times manually without high precision. By using HDR imaging one could avoid slightly under- or over-exposed images and eventually achieve higher precision in spectral reconstruction. HDR imaging has however impact on the system model and furthermore requires more sophisticated corrections for noise, for example ghosting. Many publications of the *Institute of Imaging and Computer Vision* at the *RWTH Aachen University* can be found to this topic. For reference see [8, 9, 10, 11, 12, 13, 14].

- **Detailed examination of the spectral reconstruction methods:** An evaluation of the best spectral reconstruction method should be done. We applied different kinds, for example interpolation via smoothing splines and the NNLS algorithm, and found this sufficient for the validation. However, for highly accurate measurements in the nature, one should use the reconstruction method that delivers the best results. To evaluate and compare these methods several metrics and standards have already been defined. These can be found in [1, 6, 28].

Beside these additions the system can now be put to record spectral images of natural scenes. From this a database of natural spectra can be established, which might be used by the research group for further research. It will be of great interest to follow the

progress of our multispectral imaging system in the next years and experience what else will be possible with improved technology through research.

Bibliography

[1] Hardeberg, J.: Acquisition and Reproduction of Color Images: Colorimetric and Multispectral Approaches. PhD thesis, Ecole Nationale Superieure des Telecommunications (1999) 3, 18, 20, 26, 37, 84

[2] Hardeberg, J., Schmitt, F., Brettel, H.: Multispectral image capture using a tunable filter. In: Electronic Imaging. (1999) 77–88 3, 40, 41, 42

[3] Hardeberg, J.: Multispectral color imaging. NORSIGnalet (2001) 3, 14

[4] Hardeberg, J.: Multispectral color image acquisition. In: Proceedings of the Norwegian Signal Processing Symposium (NORSIG'01). (2001) 77–82 3, 6, 7, 8, 16, 26, 41, 42

[5] Hardeberg, J.: Recent advances in acquisition and reproduction of multispectral images. In: 14th European signal processing conference, EUSIPCO, Florence. (2006) 1–5 3

[6] Cortés, A.: Multispectral Analysis and Spectral Reflectance Reconstruction of Art Paintings. PhD thesis, École Nationale Supérieure des Télécommunications (2003) 3, 18, 20, 23, 30, 33, 34, 35, 37, 44, 84

[7] Ribés, A., Schmitt, F., Pillay, R., Lahanier, C.: Calibration and spectral reconstruction for crisatel: An art painting multispectral acquisition system. Journal of Imaging Science and Technology (2005) 563–573 3, 20, 78

[8] Brauers, J., Schulte, N., Bell, A.A., Aach, T.: Multispectral high dynamic range imaging. In: IS&T/SPIE Electronic Imaging. (2008) 680704–1–680704–12 4, 84

[9] Brauers, J., Aach, T.: Longitudinal aberrations caused by optical filters and their compensation in multispectral imaging. In: IEEE International Conference on Image Processing (ICIP2008). (2008) 525–528 4, 40, 84

[10] Brauers, J., Helling, S., Aach, T.: Multispectral image acquisition with flash light sources. Journal of Imaging Science and Technology (2009) 1–22 4, 84

[11] Brauers, J., Aach, T.: Modeling and compensation of ghosting in multispectral filter wheel cameras. In: Image Analysis and Interpretation, 2008. SSIAI 2008. IEEE Southwest Symposium on. (2008) 85–88 4, 84

[12] Brauers, J., Schulte, N., Bell, A., Aach, T.: Color accuracy and noise analysis in multispectral HDR imaging. In: 14. Workshop Farbbildverarbeitung 2008. (2008) 33–42 4, 84

[13] Brauers, J., Aach, T.: Geometric calibration of lens and filter distortions for multispectral filter wheel cameras. IEEE Transactions on Image Processing (2011) 496–505 4, 84

[14] Brauers, J., Schulte, N., Aach, T.: Multispectral filter-wheel cameras: Geometric distortion model and compensation algorithms. IEEE Transactions on Image Processing (2008) 2368–2380 4, 84

[15] Quan, S.: Evaluation and Optimal Design of Spectral Sensitivities for Digital Color Imaging. PhD thesis, Rochester Institute of Technology (2002) 7, 9, 10, 37

[16] Novati, G., Pellegri, P., Schettini, R.: An affordable multispectral imaging system for the digital museum. International Journal on Digital Libraries (2005) 167–178 8

[17] Wyszecki, G., Stiles, W.: Color Science. Wiley New York (1982) 8, 9

[18] Hoffmann, G.: Cie color space. Technical report, Hochschule Emden (2002) 9

[19] Acdx: The cie 1931 xyz color matching functions. (2009) `http://en.wikipedia.org/wiki/File:CIE_1931_XYZ_Color_Matching_Functions.svg`. 10

[20] Stokes, M., Anderson, M.: A standard default color space for the internet - srgb. Technical report, W3 (1996) 10

[21] Fairchild, M.: Color Appearance Models. J. Wiley (2005) 10, 11

[22] Centroplast: Cielab (2012) `http://www.centroplast.de/de/030-Anwendungen/020-Qualitaetsmanagement/farbmessung.php`. 11

[23] CIE: Colorimetry. CIE Publication **15** (2004) 12

[24] Luo, M., Cui, G., Rigg, B.: The development of the cie 2000 colour-difference formula: Ciede2000. Color Res. (2001) 340–350 12

[25] Sharma, G., Wu, W., Dalal, E.: The ciede2000 color-difference formula: Implementation notes, supplementary test data, and mathematical observations. Color Research & Application (2005) 21–30 12

[26] Foster, D., Amano, K., Nascimento, S., Foster, M.: Frequency of metamerism in natural scenes. JOSA A **23** (2006) 2359–2372 13

[27] Urban, P.: Spectral-based image reproduction workflow (2009) 14

[28] Helling, S.: Kamerasystem und Algorithmen für die Multispektrale Farbbildaufnahme. PhD thesis, RWTH Aachen (2008) 18, 20, 23, 24, 25, 33, 37, 84

[29] Hartley, R., Zisserman, A.: Multiple View Geometry in Computer Vision. Cambridge University Press (2000) 21

[30] Pratt, W., Mancill, C.: Spectral estimation techniques for the spectral calibration of a color image scanner. Applied Optics (1976) 73–75 23, 25

[31] König, F., W., P.: A multispectral scanner (1999) 23

[32] Imai, F., Taplin, L., Day, E.: Comparison of the accuracy of various transformations from multi-band images to reflectance spectra. Technical report, Munsell Color Science Laboratory (MCSL) (2002) 28, 30, 31

[33] Burns, P., Berns, R.: Analysis of multispectral image capture. In: Proc. 4th IS&T/SID Color Imaging Conference. (1996) 19–22 29, 30

[34] D., B.P.: Analysis of Image Noise in Multitraitement Color Acquisition. PhD thesis, Rochester Institute of Technology (1997) 29

[35] Lawson, C., Hanson, R.: Solving Least Squares Problems. SIAM (1995) 31

[36] Bartels, R., Beatty, J., Barsky, B.: An Introduction to Splines for Use in Computer Graphics and Geometric Modeling. Morgan Kaufmann Pub (1987) 35

[37] Keusen, T.: Multispectral color system with an encoding format compatible with the conventional tristimulus model. Journal of Imaging Science and Technology (1996) 510–515 35

[38] Nyström, D.: Colorimetric and Multispectral Image Acquistion. PhD thesis, Linköping University (2006) 37

[39] Holst, G.: CCD Arrays, Cameras, and Displays. SPIE Optical Engineering Press (1998) 38

[40] of Circtuis Today, J.: Charge coupled devices (ccd) (2010) http://www.circuitstoday.com/charge-coupled-devices-ccd. 39

[41] Davidson, M., Abramowitz, M.: Anatomy of a charge-coupled device (2010) http://learn.hamamatsu.com/articles/ccdanatomy.html. 39

[42] McFee, C.: An introduction to ccd operation (2007) http://www.mssl.ucl.ac.uk/www_detector/optheory/ccdoperation.html. 40

[43] Brettel, H., Hardeberg, J., Schmitt, F.: Multispectral image capture across the web. In: Proc. IS&T and SID's 7th Color Imaging Conf.: Color Science, Systems and Applications. (1999) 314–316 41

[44] Beeckman, J., Neyts, K., Vanbrabant, P.: Liquid-crystal photonic applications. Optical Engineering (2011) 081202–081202 41

[45] DrBob: File:czerny-turner.png (2004) http://en.wikipedia.org/wiki/File:Czerny-turner.png. 43

[46] Optics, O.: Integrating spheres for reflectance measurements (2012) http://oceanopticsfaq.com/apps/reflectance-2/integrating-spheres-for-reflectance-measurements. 44

[47] Breton, R.: Using vrml to visualize rgb data (2012) http://www.freelists.org/post/argyllcms/Using-VRML-to-visualize-RGB-data. 45

[48] Lapez-Alvarez, M., Hernandez-Andras, J., Romero, J., Campos, J., Pons, A.: Calibrating the elements of a multispectral imaging system. Journal of Imaging Science (2009) 31102–31102 46

[49] Ferrero, A., Campos, J., Pons, A.: Experimental assessment of relative temporal fluctuation of ccd pixels. The European Physical Journal- Applied Physics (2006) 225–228 46

[50] Olsen, D., Dou, C., Zhang, X., Hu, L., Kim, H., Hildum, E.: Radiometric calibration for agcam. Remote Sensing (2010) 464–477 46

[51] Martinec, E.: Noise, dynamic range and bit depth in digital slrs (2008) http://theory.uchicago.edu/~ejm/pix/20d/tests/noise/. 49

[52] TonyTheTiger: Vignetting (2012) http://en.wikipedia.org/wiki/File:20120905_Sigma_8-16mm_f4.5-5.6_DC_HSM_lens_8mm_vignetting.JPG. 50

[53] pco.imaging: (pco.camera) http://www.pco.de/fileadmin/user_upload/db/download/MA_DCOPIE_0412b.pdf. 53, 54

[54] Allied Vision Technologies: (AVT Bigeye G) http://www.alliedvisiontec.com/fileadmin/content/PDF/Products/Technical_Manual/Bigeye/Bigeye-G_TechMan_V2.0.0_en.pdf. 53, 54

[55] Computar: (M7528-MP) http://computarganz.com/file.cfm?id=437. 53

[56] CRI (now part of PerkinElmer): (CRI VariSpec LCTF - Liquid Crystal Tunable Filter) http://www.dfisica.ubi.pt/~hgil/FotoMetria/cri/VariSpec.html. 55

[57] LOT Oriel Group: (Monochromator/Spectrograph Omni-l 150) http://www.lot-qd.de/files/downloads/gilden/eu/omni_lambda_150_eu01.pdf. 56, 57

[58] LOT Oriel Group: (10–150 W halogen source) http://www.lot-oriel.com/files/downloads/lightsources/en/halogen-lichtquelle/LQ_10___150_W_Halogen_light_source_en.pdf. 56, 57

[59] Konica Minolta: (Spectroradiometer CS-2000/CS-2000A) http://konicaminolta.com/instruments/download/instruction_manual/display/pdf/cs-2000-2000a_instruction_eng.pdf. 57, 58